universität wien

MASTERARBEIT / MASTER'S THESIS

Titel der Masterarbeit / Title of the Master's Thesis

„Strain-rate sensitivity in high pressure torsion of steel, iron and nickel“

verfasst von / submitted by

Julius Daniel Schniewind BSc

angestrebter akademischer Grad / in partial fulfilment of the requirements for the degree of

Master of Science (MSc)

Wien, 2021 / Vienna, 2021

Studienkennzahl lt. Studienblatt / degree programme code as it appears on the student record sheet:	A 066 876
Studienrichtung lt. Studienblatt / degree programme as it appears on the student record sheet:	Masterstudium Physik
Betreut von / Supervisor:	Ao. Univ.-Prof. Mag. Dr. Erhard Schafler
Mitbetreut von / Co-Supervisor:	Mag. Dr. Daria Setman

Abstract

For work hardening by plastic deformation the strain-rate sensitivity is widely accepted to be constant. However, there are few investigations of the strain-rate sensitivity at very high strain values in severe plastic deformation.

In the course of this thesis, Sandvik Bioline 316LVM austenitic stainless steel was deformed by high pressure torsion using an array of different strain-rates. The material response was recorded during the deformation process using the live applied torque. Those measurements in the form of deformation curves were analysed for their saturated state at the end of the deformation process and compared between the different strain-rates. Additionally, Vickers-hardness measurements were conducted to compare the in-situ saturated state of the sample with the sample state after relieving the pressure. To further investigate the strain-rate sensitivity, differential scanning calorimetry measurements were done to add to the comparison of the samples deformed with different strain-rates.

Not only was the data compared, but the explicit strain-rate sensitivity was calculated as well. Both the comparison and the explicit strain-rate sensitivity hint towards a deviation from the linear correlation in the logarithmic plot of stress versus strain-rate observed at lower strain-rates. Instead, the data suggests a polynomial dependence with a maximum stress achieved at a certain strain-rate and a negative strain-rate sensitivity at higher strain-rates.

Zusammenfassung

Der Einfluss der Dehnrate auf die Verfestigung von Metallen bei Kaltverformung wird im Allgemeinen als konstant angenommen. Es existieren allerdings nur wenige Untersuchungen, die sich mit dem Einfluss der Dehnrate bei Dehnungen durch Ultra-Hochverformung auseinandersetzen.

In der vorliegenden Arbeit wurde Sandvik Bioline 316LVM austenitischer rostfreier Stahl durch Hochdrucktorsion verformt. Dabei wurden verschiedene Dehnraten verwendet. Das mechanische Verhalten der Probe wurde während der Verformung anhand des anliegenden Drehmoments gemessen. Diese Messungen wurden in Verformungskurven aufgezeichnet, die jeweiligen Sättigungen am Ende der Verformungen wurden definiert und anhand der verschiedenen Dehnraten verglichen. Zusätzlich wurde mit Vickers-Härte Messungen die in-situ gemessene Spannung mit der Probenhärte nach Beendigung der Hochdruckverformung bei Umgebungsdruck verglichen. Mittels dynamischer Differenzkalorimetrie wurden weitere Unterschiede zwischen Proben, die mit unterschiedlicher Dehnrate verformt wurden ermittelt.

Neben der indirekten Analyse durch das Vergleichen der Messungen mit unterschiedlichen Dehnraten wurde der Parameter für den Einfluss der Dehnrate explizit errechnet. Beide Ansätze deuten auf eine Abweichung von dem etablierten linearen Zusammenhang zwischen den Logarithmen von Spannung und Dehnrate bei niedrigeren Dehnraten hin. Stattdessen zeigt sich eine polynomiale Abhängigkeit mit einer maximalen Spannung und einem Vorzeichenwechsel bei höheren Dehnraten.

Acknowledgements

First and foremost I would like to thank ao. Univ.-Prof. Mag. Dr. Erhard Schafler for supervising my thesis. Always having an open ear and helping any question with deep understanding and wide knowledge.

Ao. Univ.-Prof i.R. Dr. Michael J. Zehetbauer I would like to thank for constructive discussions and his help in finding relevant literature.

Special thanks to Mag. Dr. Daria Setman and Mag. Dr. Michael Kerber for their tireless help with any HPT or DSC related problem as well as many encouraging words and two amazing little whirlwinds.

Last but not least thanks to the "Evil Master Room"! Angie, Moritz, without you the daily insanity would have been half as fun (Also scientific discussions).

Contents

Chapter 1

Introduction

Severe plastic deformation is a well established technique, widely used and well understood [16–18, 26, 27].

The main characteristics of this deformation technique are the ultra-high strains achievable and exposing the deformation sample to hydrostatic pressure. Applying this method, the high target strains lead to equally high strain-rates, typically in the range of $10^{-3}s^{-1}$ to $10^{-1}s^{-1}$ [17, 26]. Putting considerably high hydrostatic pressure on metals also influences the deformation process, especially interesting in this context is the reduced defect mobility [25], probably most notable at high strains.

However there are few studies investigating the influence of high strain-rates on the HPT-deformation process and the resulting mechanical properties. At low strain-rates the strain-rate sensitivity is found to be constant [21]; the extension to a wider range of strain-rates is of principal interest. According to [19], strain-rate sensitivity is correlated to grain size where smaller grains lead to a reduction in strain-rate sensitivity. However there is no direct mention of a strain-rate influence on the strain-rate sensitivity, which will be investigated in this thesis.

With the ability to measure the live stress response during the high pressure torsion process, the strain-rate sensitivity of austenitic stainless steel 316LVM at very high strains was investigated during this thesis. The in-situ stress measurement allows direct investigation of the strain-rate sensitivity rather than approaching it indirectly [2] or via stress-rate jumps [15, 16, 20, 21].

The influence on the resulting mechanical properties were monitored by microhard-

ness indentation measurements, while the expected high defect densities as dislocations, vacancies and newly formed grain boundaries were tested by differential scanning calorimetry.

Chapter 2

Background

2.1 Crystal lattice and defects

In a crystal, the atoms are ordered in a periodic fashion. Those periodic structures are described with crystal lattices. The periodicity consists of a repetition of the smallest unit of atoms along one of the three major directions. The repeated unit is called the unit cell of a crystal. The parameters of the unit cell such as edge lenghts and angles define the crystal structure and are therefore called lattice parameters. At the same time, they define a spacial orientation for the unit cell and therefore for the surrounding crystal.

The orientation stays the same as long as the periodicity is not broken fundamentally. In a real crystal there will be areas of equal orientation called grains. The crystal-crystal interface separating those crystal phases that only differ in orientation is called a grain boundary. Since the boundary properties greatly influence grain size in a given material, which in turn is a crucial parameter for the macroscopic behaviour, grain boundaries play a central role in this thesis.

But even within the grains, the periodicity will not be perfect. There will be defects disturbing the periodicity. These can be categorised by their dimension: from point defects having "zero" dimensions to bulk defects in three dimensions.

Point defects are confined to a single point in the crystal lattice as the name suggests. The most common are vacancy defects, impurities and interstitial defects. Vacancies are lattice points where instead of the expected atom, there is a hole. If the hole is

filled by a neighbouring atom, the vacancy moves to the former site of the wandering atom, therefore moving in the opposite direction. Impurities are similar to vacancies in the sense that they replace a lattice atom. However the lattice atom is replaced by an atom not belonging in the pure crystal instead of by a hole. Lastly, interstitial impurities are atoms situated in a space between lattice points. They either carry high energies or are small compared to the crystal atoms.

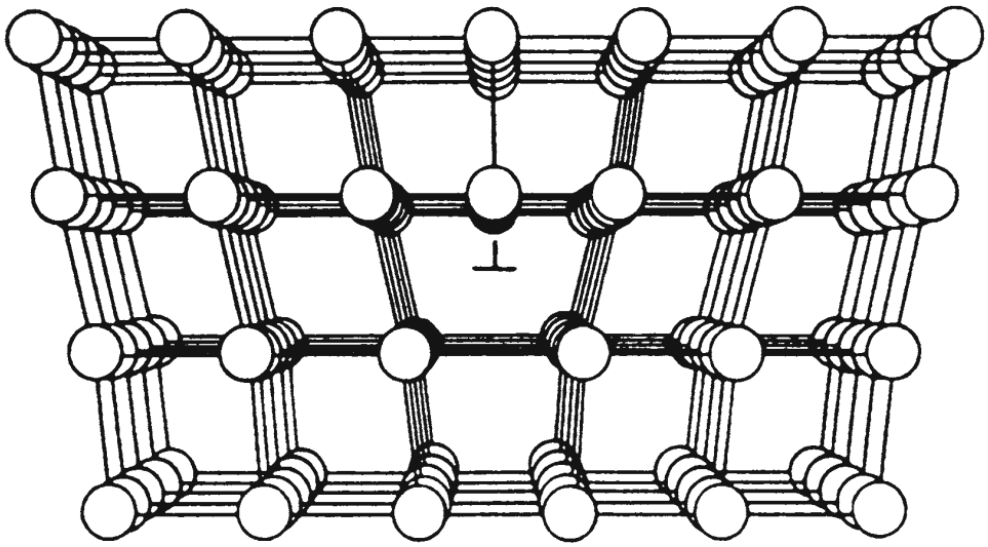

Figure 2.1: Atomic configuration of an edge dislocation taken from [6]

Onedimensional (line) defects are also called dislocations. There are immobile and mobile dislocations. In this thesis only the latter will be relevant. There are two main types of mobile dislocations, the edge and the screw dislocation. Edge dislocations can be visualised as a plane having been "inserted" halfway into a crystal with the surrounding planes bending together at the edge of the ending plane (Figure 2.1). For screw dislocations part of a crystal plane slipped one lattice point in one direction where it connects again (Figure 2.2). This results in a helix or screwlike path of atoms around the dislocation line. There are also dislocations showing edge as well as screw characteristics, these are called mixed dislocations.

Twodimensional or planar defects seperate two volumes of crystal from each other. Grain boundaries were already discussed and are the most common form of planar defects. Other defects such as stacking faults or antiphase boundaries concern stacking sequences since a stacking change always occurs on a plane between the different stacking regions.

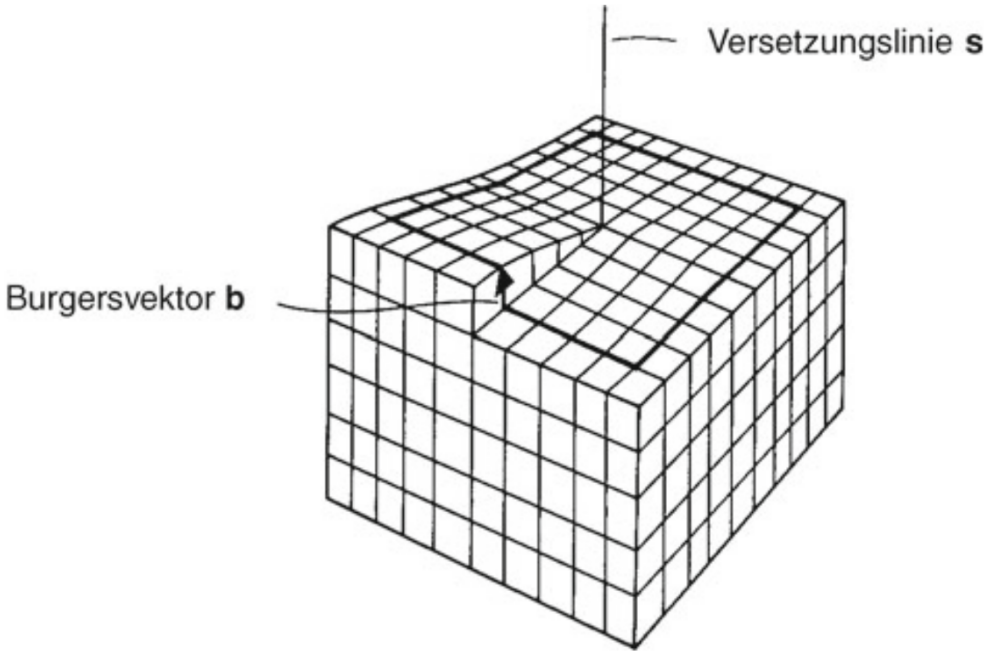

Figure 2.2: Atomic configuration of a screw dislocation taken from [6]

Bulk defects in three dimensions can be as apparent as cracks or pores but can also be vacancy clusters or precipitations.

For the effects occuring during this thesis the most important defects are mobile dislocations and to a lesser degree point defects. Planar defects will only be relevant in the form of grain boundaries while the presence of bulk defects in the samples was sought to be avoided.

None of these defects are completely stable. Depending on the temperature, they are static or mobile, which gives them a certain energy level at which they are stored. Generally the thermal stability will grow with the defects' dimension. For low dimensional defects such as vacancies and dislocations, even room temperature energy levels may be sufficient to induce mobility.

2.2 Work hardening

In the scope of this thesis, aforementioned defects were introduced into the lattice by applying strain to the crystal on a macroscopic scale. As mentioned earlier, the focus lies with dislocations. After introducing enough dislocations and thereby reaching a

suffient dislocation density, they will arrange forming new grain boundaries. This leads to smaller grain sizes in the crystal and an overall increase in hardness. This process can be divided into several stages according to the applied strain [12] and is shown in Figure 2.3.

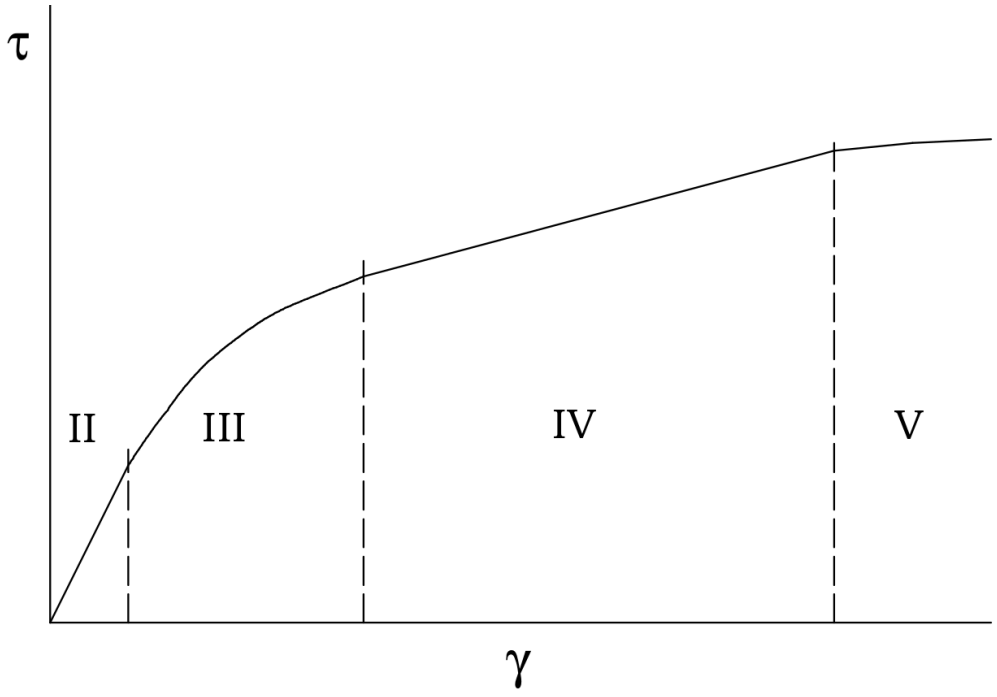

Figure 2.3: Schematic representation of the deformation curve of a polycrystal taken from [13]

Stage I only occurs in a single crystal and employs a single slip system and only stores a small number of dislocations. Stage II relaxes local critical shear stress via a secondary slip system resulting in dislocations intersecting the primary system. These stable intersecting dislocations are responsible for a rapid hardening process and act as an agglomeration point for further dislocations. Stage III shows a dynamic recovery with a characteristic $\sqrt{\epsilon}$ dependence [12]. Going to even higher strains, Stages IV and V behave analogously to stages II and III. However the dislocation cell size does not change and the dislocation density growth is significantly reduced. Zehetbauer and Seumer accredit the behaviour in stages IV and V purely to "principles of storage and annihilation for both screw and edge dislocations" [24].

2.3 Severe plastic deformation

Severe plastic deformation (SPD) is defined as a process during which large strains are imposed on a bulk work piece without significantly changing the dimensions of the sample [16–18, 26]. It can be treated as an extreme case of normal plastic deformation since the strain as well as the minimal dimensional changes are limit conditions of deformation.

SPD is a way of synthesising ultrafine-grained or even nanocrystalline structures. The term ultrafine-grained is used for grain sizes between 1 µm and 100 nm. Below that, materials are referred to as nanocrystalline. In many cases, when comparing ultrafine-grained or nanocrystalline materials with their course grained counterparts, a significant change in physical properties can be observed. In this thesis, special consideration will be given to the influence on the hardness of the material [17].

SPD is a top-down approach which starts with non-nanoscaled materials and breaks down their grains repeatedly to reach the nanoscale. Bottom-up approaches on the other hand synthesise nanoscale materials from individual atoms or molecules.

Maintaining the deformation state during and after SPD is possible because of the permanent hydrostatic pressure in the GPa range applied to the work piece. This prevents the formation of cracks and helps storing lattice defects [25].

2.3.1 High pressure torsion

There are a number of different ways to achieve SPD, such as equal channel angular pressing (ECAP) or accumulative roll bonding (ARB). In this thesis, SPD was achieved by high pressure torsion (HPT).

For HPT, a disc shaped sample is used and pinched beween two anvils as shown in Figure 2.4. By applying a load to the upper anvil, pressure is applied to the sample. Due to a sealed deformation chamber between the anvils, the sample experiences pressure which can be treated as hydrostatic.

Under pressure the sample is strained by torsion applied by rotating the anvils against each other. As a first approximation, the resulting deformation can be treated as a simple shear. An important aspect is to avoid sliding between the anvils and the sample in order to ensure the full torsional strain to be applied to the sample.

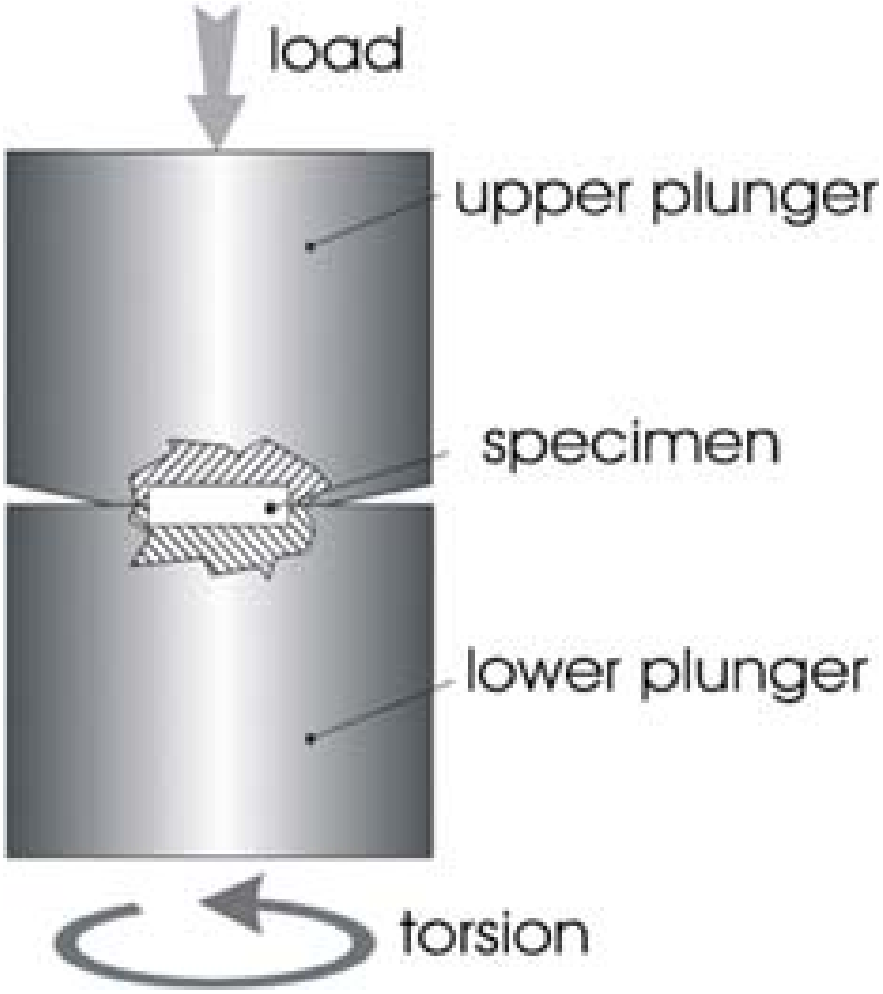

Figure 2.4: Schematic showing the HPT process with two anvils (plungers) and the sample (specimen) between them [25]

Ideally the height of the sample remains constant throughout the deformation process, however to ensure hydrostatic pressure within a sealed deformation chamber and sufficient friction between anvils and sample, the initial sample height is slightly larger than the combined depth of the anvil depressions. This results in small amounts of sample material flowing out of the deformation chamber, thereby sealing it. This reduces the sample height slightly in real experiments.

The torsional shear strain γ is given by

$$\gamma_t = \frac{2\pi r N}{t_e} \tag{2.1}$$

where r, N and t_e are the distance from the center of the sample, the number of full turns applied in the deformation process and the final thickness of the sample, respectively. To be able to compare with other strains, γ_t can be converted to the van Miese equivalent strain ϵ with

$$\epsilon = \frac{\gamma_t}{\sqrt{3}} \tag{2.2}$$

In this thesis however, γ_t will be used throughout, as only torsional strain will be considered.

To measure the real time response of the sample, the torque applied to the upper anvil by the lower anvil through the sample is measured during the deformation process. The load on the anvils and therefore the hydrostatic pressure on the sample increases the density of vacancies and dislocations by lowering their formation energy as well as suppressing their annihilation by diffusion [25].

2.4 Strain-rate sensitivity

In this thesis special attention will be paid to the strain-rate sensitivity (SRS) of HPT deformations. Strain-rate sensitivity is defined as the partial derivative

$$m = \left.\frac{\partial \ln \sigma}{\partial \ln \dot{\epsilon}}\right|_{\epsilon,T,s} \tag{2.3}$$

with σ, ϵ, T and s being stress, strain, absolute temperature and structure. For equation 2.3, ϵ, T and s are being held constant [5]. Treating stress as a function of strain, strain rate, structure and temperature,

$$\sigma = \sigma\left((\epsilon, \dot{\epsilon}, T, s\right) \tag{2.4}$$

a differential amount of stress is expressed as

$$\mathrm{d}\sigma = \left(\frac{\partial \sigma}{\partial \epsilon}\right)\mathrm{d}\epsilon + \left(\frac{\partial \sigma}{\partial \dot{\epsilon}}\right)\mathrm{d}\dot{\epsilon} + \left(\frac{\partial \sigma}{\partial T}\right)\mathrm{d}T + \left(\frac{\partial \sigma}{\partial s}\right)\mathrm{d}s \tag{2.5}$$

In order to interpret the equation in terms of SRS, both sides are multiplied by

$\dot{\epsilon}\,(\sigma\,\mathrm{d}\dot{\epsilon})^{-1}$.

$$\frac{\dot{\epsilon}}{\sigma}\frac{\mathrm{d}\sigma}{\mathrm{d}\dot{\epsilon}} = \frac{\dot{\epsilon}}{\sigma}\left(\frac{\partial\sigma}{\partial\epsilon}\frac{\mathrm{d}\epsilon}{\mathrm{d}\dot{\epsilon}} + \frac{\partial\sigma}{\partial\dot{\epsilon}} + \frac{\partial\sigma}{\partial T}\frac{\mathrm{d}T}{\mathrm{d}\dot{\epsilon}} + \frac{\partial\sigma}{\partial s}\frac{\mathrm{d}s}{\mathrm{d}\dot{\epsilon}}\right) \tag{2.6}$$

Using

$$\frac{\mathrm{d}x}{x} = \mathrm{d}\ln x \tag{2.7}$$

equation 2.6 becomes

$$\frac{\mathrm{d}\ln\sigma}{\mathrm{d}\ln\dot{\epsilon}} = \frac{\partial\ln\sigma\ \mathrm{d}\epsilon}{\partial\epsilon\ \mathrm{d}\ln\dot{\epsilon}} + \frac{\partial\ln\sigma}{\partial\ln\dot{\epsilon}} + \frac{\partial\ln\sigma\ \mathrm{d}T}{\partial T\ \mathrm{d}\ln\dot{\epsilon}} + \frac{\partial\ln\sigma\ \mathrm{d}s}{\partial s\ \mathrm{d}\ln\dot{\epsilon}} \tag{2.8}$$

With equation 2.3 and

$$\gamma = \frac{\partial\ln\sigma}{\partial\epsilon}\ \text{(incremental strain hardening rate)}$$
$$\delta = \frac{\partial\ln\sigma}{\partial T}\ \text{(incremental temperature sensitivity of stress)}$$
$$\theta = \frac{\partial\ln\sigma}{\partial s}\ \text{(incremental structure sensitivity of stress)}$$

equation 2.6 becomes

$$m_{app} = \gamma\frac{\mathrm{d}\epsilon}{\mathrm{d}\ln\dot{\epsilon}} + m + \delta\frac{\mathrm{d}T}{\mathrm{d}\ln\dot{\epsilon}} + \theta\frac{\mathrm{d}s}{\mathrm{d}\ln\dot{\epsilon}} \tag{2.9}$$

This shows the importance of only slight changes in the experimental conditions since the true SRS will be influenced by each of the parameters.

Equations 2.3 to 2.9 as well as the derivations are taken from [5].

2.5 Hardness measurements

In order to verify the strengthening effects and to compare the in-situ torque measurements with the sample state after releasing the hydrostatic pressure of HPT, hardness measurements are necessary. Hardness measurements are non destructive in the scope of this thesis, preserving the deformation state of the sample. A square based pyramidal (Vickers-) indenter is perpendicularly forced into the sample surface with a defined load. The hardness is defined as

$$\sigma = \frac{F}{A_{Ind}} \tag{2.10}$$

where F and A_{Ind} are the applied load and the contact surface between the indenter and the sample respectively. If the contact area is observed with a light microscope, only the projected area can be measured. In combination with the known shape of the Vickers indenter, equation 2.10 becomes

$$\sigma = \frac{2 \cdot \sin\left(\frac{136°}{2}\right)}{\left(\frac{d_1+d_2}{2}\right)^2} \cdot F \tag{2.11}$$

with d_1 and d_2 being the measured diagonal lengths of the projected area.

2.6 Differential scanning calorimetry

Differential scanning calorimetry (DSC) is a technique in which a sample is annealed in a very controlled way. Thus it is a destructive measurement technique for samples with a significant deformation history. It is a powerful tool sensitive to the activation enthalpies of different defects such as vacancies and dislocations. In general terms, an energy level can be appointed to different deformation processes.

For the actual measurement, the sample and a control material are simultaneously heated up to a set temperature while being kept at the same temperature at all times. The necessary energy to achieve this is being recorded. As soon as a change in the sample takes place (e.g. annealing of defects from deformation processes), the required energy will be different between the sample and the control material. This difference gives a heat flow curve. The area under this curve in turn gives the enthalpy of the

process taking place in the sample. That way, every group of defects will be annealed at their own energy level and can usually be seperated well enough.

Chapter 3

Experimental Procedures

In this chapter, materials used in the course of this thesis as well as the procedures those materials underwent will be discussed. This will be done in chronological order so as to follow the experimental path from raw material to the final data.

3.1 Materials

The central material of this study is Sandvik Bioline 316LVM austenitic stainless steel. This is a low-carbon, vacuum-melted 316L grade stainless steel, UNS S31673 certified to ASTM F138, supplied as annealed in the form of 50 mm diameter rods, with the chemical composition in weight $0.023C - 0.6Si - 1.7Mn - 17.5Cr - 13.5Ni - 2.8Mo$ [8]. For use in HPT experiments, the steel was already processed into rods of 8 mm diameter which were used in this thesis. Preliminary measurements were done with pure nickel and pure (ARMCO) iron in order to gauge sensible parameter ranges for the central experiments. These were supplied as pellets and 8 mm diameter rods respectively.

3.2 Sample preparation

The first task was to prepare the samples in the state that was to be investigated. This was done in multiple steps. For use in HPT, a disc of a set diameter and height is needed depending on the anvils used in the experiment. Manufacturing these is the first task of sample preperation and was mainly done by spark erosion.

3.2.1 Spark erosion and heat treatment

In order to use spark erosion, either the height or the diameter already has to be equal to the desired sample dimensions. The steel and iron rods had the desired diameter, so for these no further preperation was needed, whereas the nickel pellets had to be rolled into the desired height to proceed.

With the equipment available for spark erosion, either cutting or punching is possible. In both cases the work piece and a cutting tool are oppositely charged and submerged into a dielectric fluid. With increasing voltage or shrinking distance between the two electrodes, the voltage will discharge into a current and thereby some material is removed from the electrodes. This technique enables strainfree cutting or punching and is therefore commonly used when dealing with materials in defined stress states.

The iron rod was cut into discs by using a running wire as the cutting tool. There were complications due to wire breaking and actual contact between the wire and the work piece, both leading to an interruption of the cut. Approximately nine out of ten of these interrupted cuts could not be resumed due to the cut closing itself up again, trapping the wire. Every cut, the successful as well as the failed ones, took about sixty minutes. For cutting steel, the same procedure took place with the only difference being the duration of the cuts, steel took around ninety minutes to cut. In both cases the success rate was lower than expected, approximately 65% for iron and 50% vor steel. The reason for the failed cuts could not be pinpointed. The only hint is the difference between iron and steel, where the steel is significantly harder than pure iron.

Nickel was punched after having been rolled to the appropriate height. Spark erosion punching did not present any complications.

This way all three materials were shaped into discs of 8 mm in diameter and 0.85 mm height. Due to the cutting process the sample height was not completely equal among the samples, but since HPT procedure reduces the height further (section 2.3.1), this is of no concern for the results. Furthermore most of the samples were in the range of $0.85 \pm 0.05 mm$ as measured after cutting. Those differences had no observable influence on the post deformation state.

To ensure the purity of the deformed material, traces of the wire material needed to be removed with diluted nitric acid. Early samples were prepared without this step and showed surface impurities presumed to stem from the wire material.

To be able to start the deformation from an undeformed state, the sample discs were then heat treated in vacuum or under protective argon athmosphere for complete annealing. Either athmosphere proved to be working equally well in preventing oxidation of the sample surface. The iron and steel discs were heated to 700 °C for 2 h and the nickel discs were heated to 640 °C for 2 h. Despite using a protective athmosphere during heat treatment, a soot layer formed on the sample surface. This was removed with diluted nitric acid in the beginning, lateron simply grinding the soot layer off was found to be a much faster and easier procedure with the same effect.

This preparation was performed for all samples used in this thesis. It erases potential prior deformation history and results in samples with randomly distributed grain orientation. This way, all samples of the same material can be assumed to be equal before deformation.

3.2.2 High pressure torsion

Since the functionality and principle of HPT has been explained in section 2.3.1 the focus in this chapter will be on the execution of the deformation experiments.

Prior to deforming any sample, it must be sandblasted along with the anvil cavities to ensure a sufficient microroughness on all surfaces. This, along with the samples at a height of 0.85 mm being larger than the chamber at a height of 0.6 mm, drastically reduces the risk of sliding between anvils and sample during the deformation process. In case of the HPT machine used for this thesis, the lower anvil is rotated while the upper anvil remains stationary. In order to monitor the live response of the sample, the torque applied to the upper anvil is measured continuously during the deformation process.

Special care must be taken when setting up the anvils in order to have them perfectly aligned to each other. If one is tilted in regard to the other, the stress experienced by the sample will not be uniform but angle dependent. Since this is not part of the model used in section 2.3.1, it was treated as a systematical error.

All samples were deformed at a pressure of 4 GPa for two full turns. In order to investigate the influence of the strain-rate on the deformed state of the sample, samples were deformed at different deformation speeds. To statistically strengthen the results, four or more samples were deformed at each deformation speed. To be able to gauge a sensible range of strain-rates, iron and nickel as prominent representatives of the

Rotation speed $\left[\frac{rot}{min}\right]$	Rotation speed $\left[\frac{rot}{sec}\right]$	strain-rate at $r = 4mm$ $\left[\frac{1}{s}\right]$
0.02	0.000333	0.01396
0.2	0.003333	0.13963
2	0.033333	1.39626

Table 3.1: Anvil rotation speeds and strain-rates in the preliminary experiments with pure iron and pure nickel; strain-rates were obtained by dividing the calculated maximum applied strain by the deformation time

Rotation speed $\left[\frac{rot}{min}\right]$	Rotation speed $\left[\frac{rot}{sec}\right]$	strain-rate at $r = 4mm$ $\left[\frac{1}{s}\right]$
0.01	0.000167	0.00698
0.06	0.001	0.04189
0.1	0.001667	0.06981
0.6	0.01	0.41888
1	0.016667	0.69813
6	0.1	4.18879

Table 3.2: Anvil rotation speeds and strain-rates in the experiments done with Sandvik steel; strain-rates were obtained by dividing the calculated maximum applied strain by the deformation time

lattice types bodycentered cubic and facecentered cubic respectively were deformed. For these preliminary measurements, the measured strain-rates were chosen as shown in table 3.1, spanning a range of two orders of magnitude.

After assessing the results of the preliminary measurements as will be discussed in section 4.3.1, steel samples were deformed with six different strain-rates, five each at least, according to table 3.2. The changing parameter in the deformation experiments was the rotation speed of the lower anvil.

At the highest strain-rate, the deformation only took 20 seconds, while deforming at the lowest strain-rate took 3 hours and 20 minutes. Some of the samples deformed at the highest strain-rate were prone to slips and other artifacts in the stress-strain curve making those samples not usable in the further course of the study. Thus, deformations needed to be repeated in order to ensure a sufficient amount of deformations at a given speed for a statistically sound result.

3.3 Analysis Methods

In the process of sample preparation, generally no data is obtained for analysis. HPT is an exception to this. Despite transforming the sample into the desired deformation state, the torque measurement conducted during the process can already be used to gain insights regarding the deformation.

3.3.1 Analysis of measurement uncertainties during HPT

To be able to evaluate the deformation data, possible measurement uncertainties must be discussed first.

Piston position

As was described in section 3.3.2, stress-strain curves were used to analyse the deformation process. Since the position of the piston during the process was recorded in full degrees, the resulting stress showed discrete values rather than a continuous flow. Especially in the slower deformations, timespans of up to twenty seconds therefore showed no change in stress. In order to be able to investigate the shear stress in finer steps, the recorded turning speed was used to calculate the real position for every measurement interval using the recursive formula:

$$x(n+1) = x(n) + \dot{\phi}(n) \cdot 50\,\mathrm{ms} \tag{3.1}$$

with $x(n)$ being the position at measurement point n and $\dot{\phi}(n)$ being the turning speed at the same measurement point in $\frac{^\circ}{s}$. Having refined the data of one measurement, it was compared to the original data set. Figure 3.1a shows the manipulated data set in magenta over the untreated set in black. Comparing both graphs shows two major differences.

At small strains (figure 3.1b), a difference is noticable since the start of the deformation exhibits large stress changes with little strain change. Additionally, the deformation does not start at full speed but rather needs to accelerate in the first 2-3 seconds.

The second noticable difference between both sets of data is the slightly higher strain shown in the data with finer piston positions. Due to rounding errors adding up over the course of the recursion, instead of 720° the final position adds up to 725.5° and

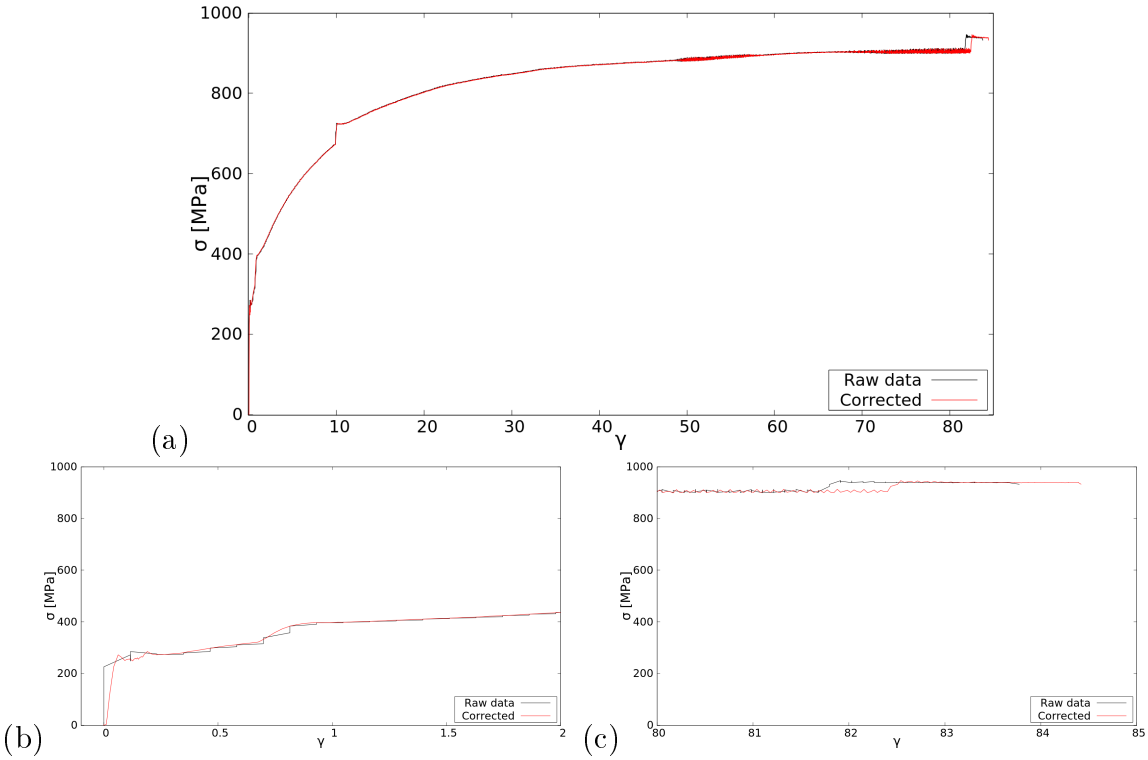

Figure 3.1: Comparison between raw anvil position data and position data obtained from momentary rotation speed displayed (a) in total, (b) at low strains, (c) at high strains

therefore shows a higher strain as can be seen in Figure 3.1c.

Overall those two differences do not warrant the usage of the finer piston positions. The low angle differences are negligible since the focus in this thesis lies on the stable saturation state. The high angle difference even adds errors from the rounding in the recursion. Thus for the rest of the thesis, the unmanipulated position data will be used in the stress-strain curves.

Torque measurements

To evaluate the uncertainty in the torque measurements, 450 data points were recorded at a constant pressure of 2 GPa without rotation. The obtained data was analysed to find the data in equation 3.2 with σ being the sample standard deviation.

$$\begin{aligned} Q_{Max} &= 0.08529\ \frac{mV}{V} \\ Q_{Min} &= 0.08448\ \frac{mV}{V} \\ \bar{Q} &= 0.08489\ \frac{mV}{V} \\ \sigma_Q &= 0.00014\ \frac{mV}{V} \end{aligned} \tag{3.2}$$

Using Gaussian error propagation, the standard deviation of the calculated stress was calculated to be $\sigma_\tau = 0.6387\,\mathrm{MPa}$. As such, the error in correlation to saturation values is below one per mille and is not displayed in the following figures.

3.3.2 In-situ stress measurements

As was already mentioned in section 3.2.2, the torque applied to the upper anvil by rotating the lower anvil is continuously recorded during the deformation process. Along with the position of the lower anvil, the current turning speed, the load on the sample and the piston pressure, the torque is registered every 50 milliseconds.

The torque tool used for measuring is shown in Figure 3.2. The principle behind the measurement is a Wheatstone bridge with strain gauges in place of the resistors. That means four strain gauges would make a full Wheatstone bridge. For torque measurements with pure torque at a 45° angle, special half bridge strain gauges can measure the opposing directions. They also enable eliminating pressure and tensile strain components. For Figure 3.2, a small tilt during compression with applied torque can easily occur. This results in an oscillating torque signal. In order to minimise this effect geometrically and to increase the total signal, rather than two half-bridges, four bridges each displaced 90° around the axis of rotation are used in Figure 3.2. This also allows for correcting vertical placement errors by placing the four bridges in an alternating up/down configuration. These tools are very well aligned to the rotational axis and their top and bottom allow for a highly precise angular positioning which further decreases any errant compressive or tensile components.

Having the neighbouring quarter bridges corresponding to the same strain component connected in series not only averages but amplifies the signal resulting from the torque on half of the shaft.

Figure 3.2: Photograph of the installed torque tool

The corresponding diagram is shown in Figure 3.3. It shows the strain gauges alternately reacting with increase or decrease of resistance to strain but having the same resistance in the relaxed state, making the bridge a balanced one. That way, the signal voltage V_S is calculated as

$$V_S = \frac{V_0}{4 \cdot R} \cdot (\Delta R_1 \cdot \Delta R_2 \cdot \Delta R_3 \cdot \Delta R_4) \tag{3.3}$$

with the initial voltage V_0, the initial resistance of the strain gauges R and the change in resistance at each individual gauge ΔR_n.

Minimalising the influence on the output, the excitation voltage V_0 is applied on the longer legs connected to the bottom of the tool, while the signals are taken from the shorter upper connectors. In case of an imbalance due to the manufacturing process of the gauges, the tool can be zero-adjusted by a shunt resistor connected parallelly on one side of the Wheatstone bridge. For the tool used, the physical asymmetry of the bridge is below 0.2% of the typical signal levels measured in this thesis.

A load correction curve was recorded as well. It shows an influence well below the

noise level but also less than 1% of the typical signal level. All data is corrected for this effect but shows no visible deviation of the data.

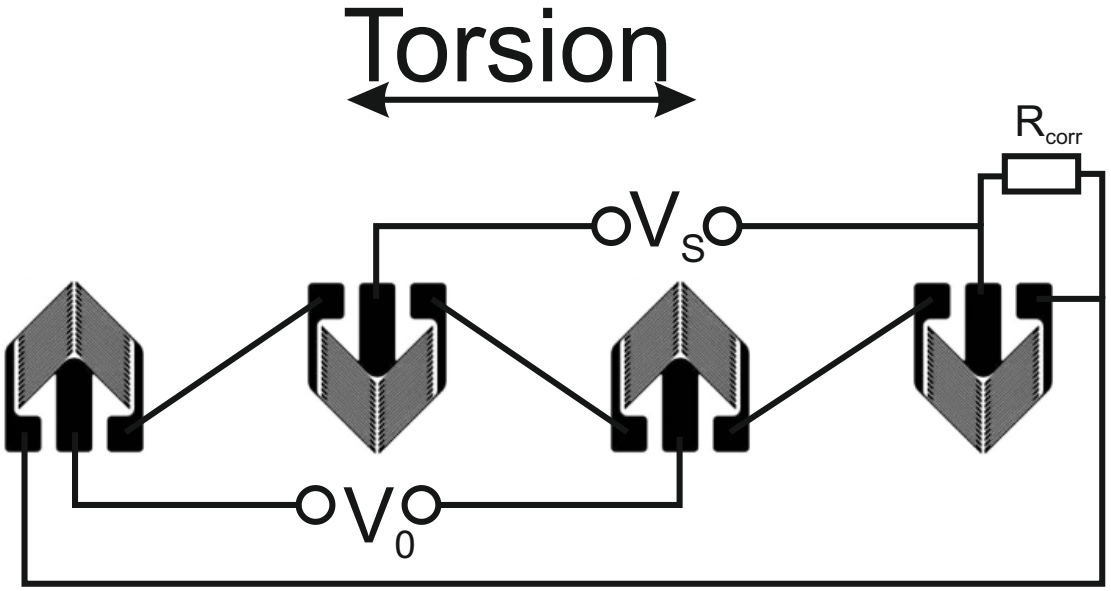

Figure 3.3: Circuit diagram of the installed torque tool

The torque on the upper anvil can directly be interpreted as the response of the sample to the applied strain. Usually, the torsional stress rather than the torque will be considered, so the sample response (or hardening curve) is shown and analysed in this thesis as a stress-strain curve (Figure 3.1a). It plots stress versus strain with the torsional shear strain γ as defined in equation 2.1 and the stress τ as

$$\tau = \frac{3 \cdot Q}{2\pi \cdot r^3} \tag{3.4}$$

with Q and r being the applied torque and the sample radius respectively.

In order to compare the deformation curves obtained at different strain-rates, a saturation curve with the formula

$$\tau = (\tau_{max} - \tau_0) \cdot \left(1 - e^{-kx}\right) + \tau_0 \tag{3.5}$$

with τ_{max} being the saturation stress, τ_0 the y-axis intersection and k the exponent's factor is used. Usually, a saturation curve starts at the origin and therefore τ_0 would not be needed. However since the rotation angle of the lower anvil can only be recorded

in full degrees, all data recorded during the first degree of rotation is correlated with a strain of 0. Therefore the correcting parameter of τ_0 was introduced into the saturation curve formula. With this, the saturation value τ_{max} as well as the onset of the deformation were comparable between the different strain-rates.

The similarity of the deformation curves in the sample groups having been deformed with the same strain-rate was evident apart from slip artifacts. The small spread in onset as well as in saturation stress made it possible to concentrate on one representative sample from each group for further analysis.

3.3.3 Saturation fits

After having established the reliability of most measurements, the reliable data were fitted to the saturation formula explained in section 3.3.2. One exemplary fit is shown in Figure 3.4, all fits can be found in appendix A. Having intentionally chosen an example with two prominent jump artifacts and an incline at high strain values, the fitted function still represents the saturation level very accurately. Especially jump artifacts in the saturation range are corrected consistently in the expected way. Given the explanation in section 4.2.1, the pressure before the artifact fell below a certain threshold and was then increased. Comparing different curves from equivalent deformations suggests that the pressure level after the artifact is in fact higher than the desired pressure of 4 GPa. The real value at the artifact site itself is therefore expected to be between the two levels of the jump. The difference between those levels however translates into uncertainties of the saturation values.

To estimate the upper bounds of the systematical errors, the height of the jump artifacts was determined and then halved since the real value is expected to be between the two levels of the jump. As a basis for this estimation, ten jump artifacts in the saturation range from different measurements were analysed. Since this was done in order to bind the systematic error from above, the greatest analysed jump was taken as a reference. This sets the uncertainty of the fitted saturation stress values to 20 MPa as is shown in equation 3.6.

$$\Delta\sigma = \frac{1}{2} \cdot \text{jump height} = \frac{1}{2} \cdot 39.43\,\text{MPa} < 20\,\text{MPa} \tag{3.6}$$

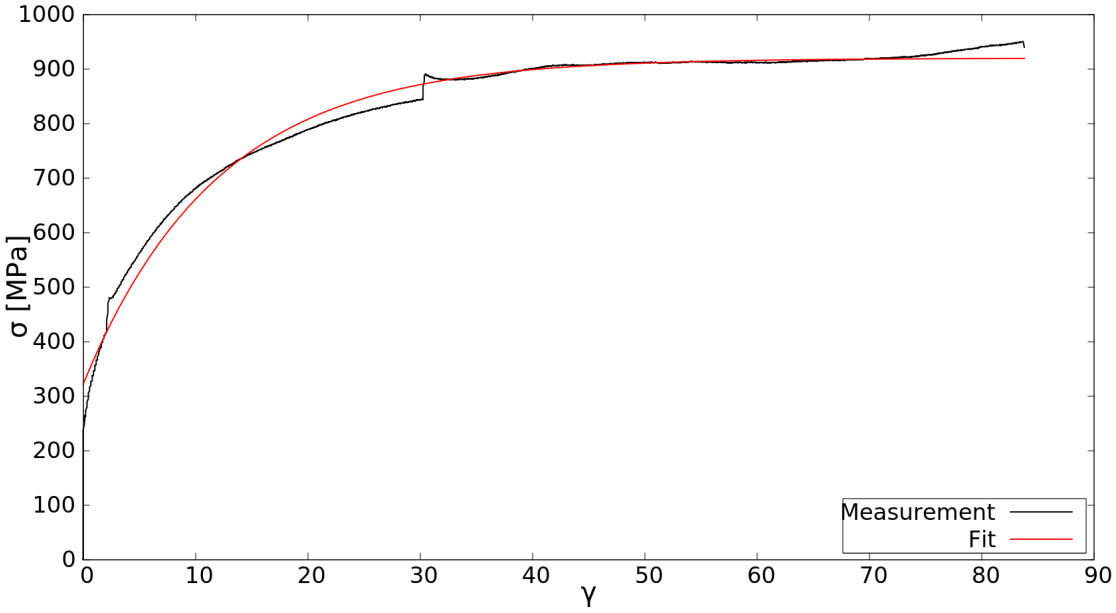

Figure 3.4: Saturation curve fitted to stress-strain curve 2 from 4.6

Radius $[mm]$	strain-rate for $1\frac{rot}{min}$ $\left[\frac{1}{s}\right]$	strain-rate for $6\frac{rot}{min}$ $\left[\frac{1}{s}\right]$
0.63	0.101	0.660
2	0.349	2.094
3.25	0.567	3.403
3.8	0.663	3.979

Table 3.3: HV measurement sites and corresponding strain-rates for two rotation speeds

3.3.4 Microhardness

After releasing the pressure from HPT, the samples reached their final stable state. An important parameter to evaluate that state is hardness. To be able to rely on the data obtained from the hardness measurements, each sample was measured multiple times on several radii.

However, before being able to conduct hardness measurements, the samples needed to be ground and polished to produce a surface smooth, even, and clean enough to be able to make undisturbed indentations as described in section 2.5.

After achieving a surface suitable for hardness measurements, the hardness was measured on different radii according to the strain-rate $\dot{\epsilon}$ as is shown in table 3.3.

The measurement radii were selected in such a way so as to be able to compare hardness between the different rotation speeds. As table 3.3 shows, the strain-rate at $r =$

0.63 mm and 6 $\frac{\text{rot}}{\text{min}}$ is comparable to the strain-rate at $r = 3.8\,\text{mm}$ and 1 $\frac{\text{rot}}{\text{min}}$. In the same manner, the strain-rate at $r = 2\,\text{mm}$ and 1 $\frac{\text{rot}}{\text{min}}$ is comparable to the strain-rate at $r = 3.25\,\text{mm}$ and 0.6 $\frac{\text{rot}}{\text{min}}$. Additionally, every radius of every sample was measured ten times to be able to obtain the mean value at any given radius instead of relying on a single measurement.

These ten measurements per radius were not done in a single spot but rather along a circular line with the radius of the current measurement and at least one millimeter distance between indentations. This was done to check whether the sample shows the same hardness in all directions, thus making sure the sample was deformed homogeneously.

3.3.5 Differential scanning calorimetry

Since DSC is a destructive measurement technique in the scope of this thesis as was explained in section 2.6, the measurements were conducted last. Each of the samples was measured against an annealed sample of the same material.

Depending on material and temperature range, phase changes can take place during a DSC measurement. Those however can be isolated by running the same heating-cooling cycle twice in a row with the same sample. The effects showing in both cycles can be attributed to processes other than deformation and can therefore be neglected in the scope of this thesis.

Data obtained from the DSC are a peak temperature and the area of each peak A_P as can be seen in 3.5. The temperature allows appointing an energy level to the annealed dislocations via their activation enthalpy. The peak area allows calculating the energy stored in them per volume which is given as equation 3.7 with G, b, N and κ being the shear modulus, the Burgers vector, the dislocation densitiy and $\kappa = \frac{1+(1-\nu)}{2}$ the (equal) ratio of edge and screw dislocations with the Poisson ratio ν respectively.

For this thesis the higher temperature peak is of interest, since dislocations anneal at the highest temperature [11] [10] [4] and dislocations are the main concern when dealing with stage IV and V. The energy stored in the dislocations is given as

$$E_{stor} = G\,b^2\,\frac{N}{4\pi\kappa}\,\ln\left(\frac{1}{b\,\sqrt{N}}\right) \tag{3.7}$$

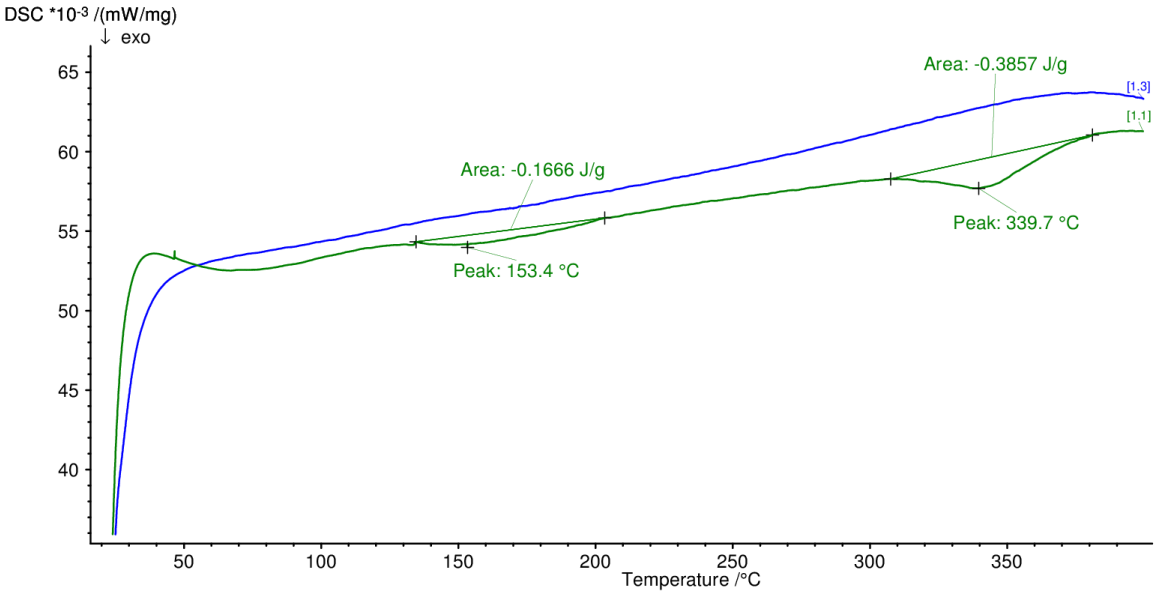

Figure 3.5: DSC measurement done with Sandvik steel deformed at 4 GPa for 2 turns at $6\frac{rot}{min}$

with G being the shear modulus, b the absolute value of the Burgers vector and N the dislocation density. $\kappa = \frac{2-\nu}{2}$ is the mean of 1 and $(1-\nu)$, with the Poisson ratio $\nu = 0.33$. This assumes equal parts screw and edge dislocations.

In the context of DSC however, the stored energy can be calculated as is shown in equation 3.8 with the sample mass m and the sample volume V.

$$E_{stor} = A_P \cdot \left(\frac{m}{V}\right) \tag{3.8}$$

With equation 3.7 and equation 3.8, the dislocation density N can be calculated.

Since the analysis software does not give an uncertainty, for both obtained values an uncertainty was estimated based on the method of analysis. The peak temperature was found by searching for the minimal value in an area selected by hand. Its uncertainty is connected to the uncertainty of the temperature measurement and the peak temperature was therefore assumed to be accurate within 3 °C. The peak area was calculated by appointing a starting point and an end point. The software draws a line between the two points and calculates the area between the curve and the line. Since there is quite a margin in the placement of the points, two extreme point placements were

compared and the error was estimated by the resulting difference in peak area. Thus, the uncertainty for the peak areas is estimated to be $0.05\,\frac{\mathrm{J}}{\mathrm{g}}$. To be able to estimate the uncertainty of the calculated dislocation density, the extreme values were calculated for each dislocation density. These deviations were taken as a low estimate since the lattice constant of pure iron was used in the calculations. This incurs further uncertainty due to the composition of the Sandvik steel and therefore a slightly different lattice constant.

Chapter 4

Results and Discussion

4.1 Stages of work hardening

Rotation speed	Stage II $[GPa]$	Stage IV $[GPa]$	Ratio
0.01	0.392 ± 0.101	0.061 ± 0.007	0.155
0.06	0.369 ± 0.095	0.059 ± 0.001	0.161
0.1	0.312 ± 0.013	0.06 ± 0.002	0.193
0.6	0.307 ± 0.024	0.06 ± 0.003	0.195
1	0.325 ± 0.032	0.061 ± 0.003	0.189
6	0.42 ± 0.22	0.076 ± 0.031	0.181

Table 4.1: Hardening rates in stages II and IV with their respective ratio

After conducting the HPT deformations, the stages of work hardening detailed in [12] were observed in the deformation curves. Special attention was given to stages II and IV and their comparison. With the high strains reached in the deformation, stage II takes place in the first 10° of the deformation process, while stage IV is prevalent to the deformation process between 10° and 100°. In order to investigate both stages and the influence of strain-rate on them, linear approximations were done and the hardening rates were compared.

To illustrate, Figure 4.1 shows the area of stage II and the transition to stages III and IV. The hardening rates $\frac{\partial \tau}{\partial \gamma}$ were obtained for each strain-rate by linear approximation. According to [12], stage II is correlated with a hardening rate in the dimension shown in equation 4.1 taken from 4.1. Here, μ is the shear modulus of the deformed material.

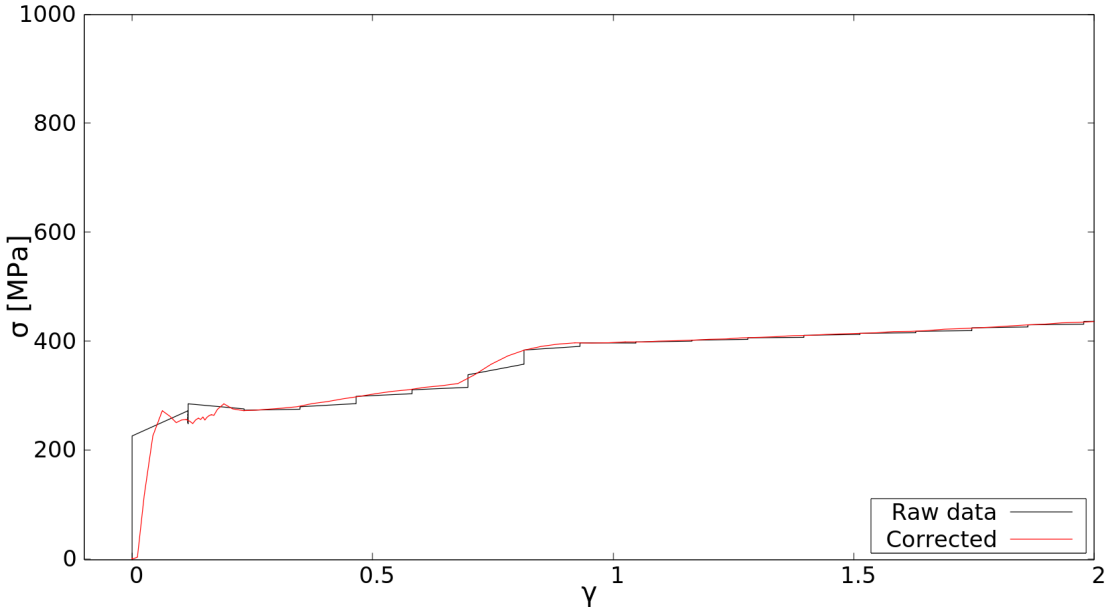

Figure 4.1: Close-up of the deformation in the area of $0 \leq \gamma \leq 1$

$$\frac{\mu}{200} = \frac{70.3GPa}{200} = 0.352GPa \tag{4.1}$$

That dimension seems in accordance with the data from table 4.1. Comparing stages II and IV shows a change with strain-rate. With increasing strain-rate, the ratio first increases from 15.5% to 19.3% and decreases at high strain-rates again to 18.1%. This suggests a non-linear dependency of the deformation process on the strain-rate.

4.2 Preliminary measurements

The preliminary measurements of pure iron and nickel were undertaken as to acquire stress-strain curves and Vickers hardness values.

4.2.1 Stress-strain curves

Figure 4.2 shows three stress-strain curve measurements done with pure iron at 0.02, 0.2 and 2 rotations per minute $\left[\frac{rot}{min}\right]$. The curves show an immediate steep increase in stress at low strain values. This manifests itself as a general characteristic of all stress-strain curves throughout the thesis. The stress keeps rising at a decreasing rate until a saturation is reached at high strain values. This turns out to be the second

general characteristic of stress-strain curves.

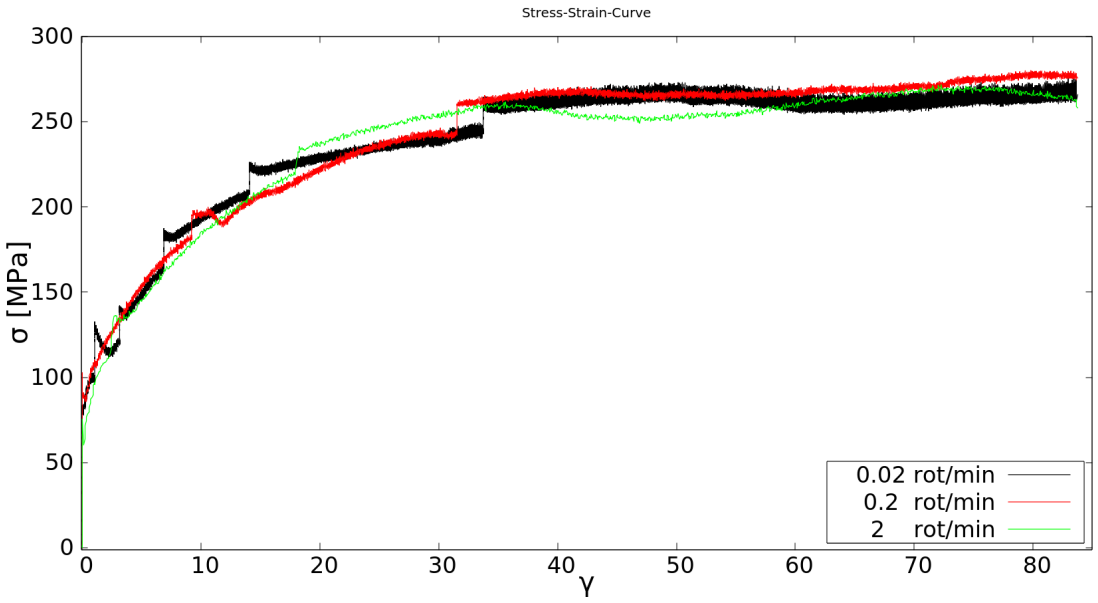

Figure 4.2: Three representative stress-strain curves obtained from HPT deformation of pure iron for 2 rotations at 4 GPa with 2 $\frac{rot}{min}$, 0.2 $\frac{rot}{min}$ and 0.02 $\frac{rot}{min}$

A striking difference between the curves recorded at different rotation speeds is the point density of the curves. This can easily be explained since the measurement time interval remains constant while the measurement time itself increases with decreasing rotation speed. This leads to a factor of 100 between the amount of measurement points in the curve recorded at 0.02 $\frac{rot}{min}$ as compared to the one recorded at 2 $\frac{rot}{min}$. This is true for all measurements at slower rotation speeds. Since it translates to measurement point density, the "thickness" has no influence on the further analysis of the data.

There are some artefacts in each stress-strain curve where the stress suddenly jumps up. Their number ranges mostly between two and five and they tend to occur more frequently with lower deformation speed. These artefacts mark points at which the hydraulic pressure regulation needed to re-increase pressure to maintain the desired pressure of 4 GPa. Since the undeformed samples need to have a slightly larger volume than the deformation chamber, as was explained in section 3.2.2, minimal amounts of material flow out of the chamber, reducing the pressure inside. Thus, each time the pressure falls under a certain threshold, the pressure is re-increased again, leading to a jump in stress. An attempt to remove each artefact individually proved to be impractical and did not deliver reliable data. Because multiple data points before and

after the artefact were affected in a non traceable way, the individual artefacts were not corrected. However a different approach for correction was chosen and will be discussed in section 4.3.2.

Comparing the representative stress-strain curves shown in Figure 4.2, the focus is the saturation value of the deformation, since the stable state is to be compared. The direct comparison shows 2 $\frac{rot}{min}$ having the lowest and 0.2 $\frac{rot}{min}$ having the highest saturation value. This trend is true for all iron deformations conducted in the course of this thesis.

The visual analysis is impeded by the overlying oscillation most prominently showing in the saturation. This was found to be caused be a slight angle between the anvils leading to different torque values depending on the rotation angle. Having identified this problem through the preliminary measurements, it was significantly less prominent in the steel experiments after adjusting the experimental setup and gaining experience with handling the anvils during each experiment.

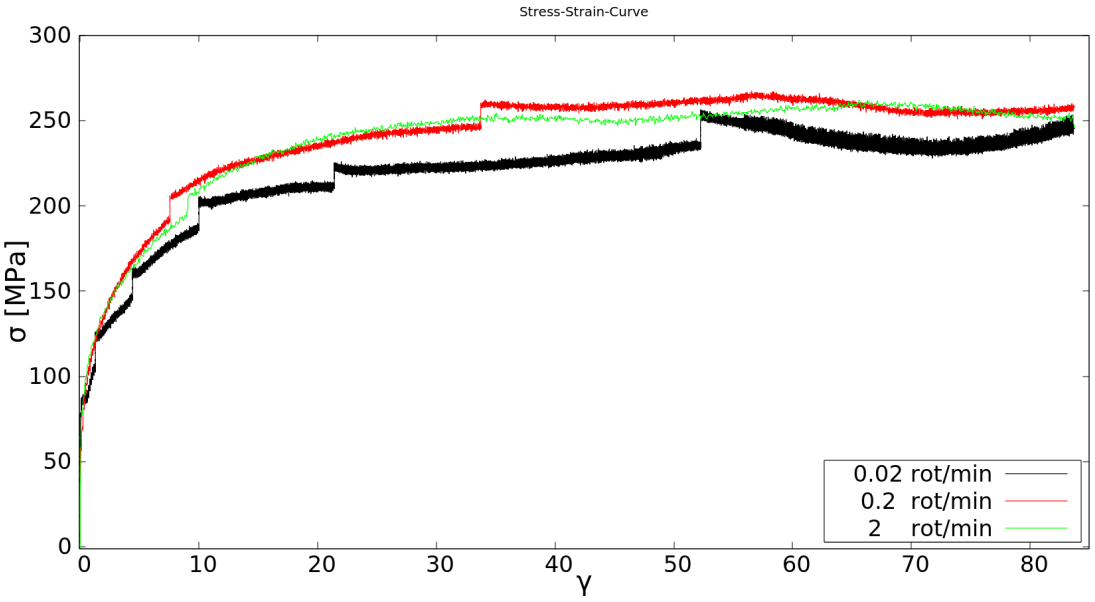

Figure 4.3: Three representative stress-strain curves obtained from HPT deformation of pure nickel for 2 rotations at 4 GPa with 2 $\frac{rot}{min}$, 0.2 $\frac{rot}{min}$ and 0.02 $\frac{rot}{min}$

In Figure 4.3, three representative curves of the nickel deformations are displayed. All curves again show a significant overlying oscillation and their saturation values are very close to each other. 0.2 $\frac{rot}{min}$ again shows the highest value. In this case the curve resulting from the deformation with 0.02 $\frac{rot}{min}$ is behaving differently from the others; in the range of $10 \leq \gamma \leq 50$ the stress values are smaller than expected. One possible

reason is the aforementioned imprecise pressure control. This is supported by the fact that after a large artefact at $\gamma = 52.25$, the values are comparable again.

Figure 4.2 as well as Figure 4.3 show saturation values in the same range. However, comparing the curves stemming from 2 $\frac{rot}{min}$ and 0.2 $\frac{rot}{min}$ in Figure 4.4, there are some differences. 0.02 $\frac{rot}{min}$ curves were not included here to avoid cluttering the figure. While both nickel curves exhibit a steeper onset than the iron curves, the iron curves show higher saturation values. This hints at faster hardening of nickel at low strain values while iron undergoes more hardening at higher strain values.

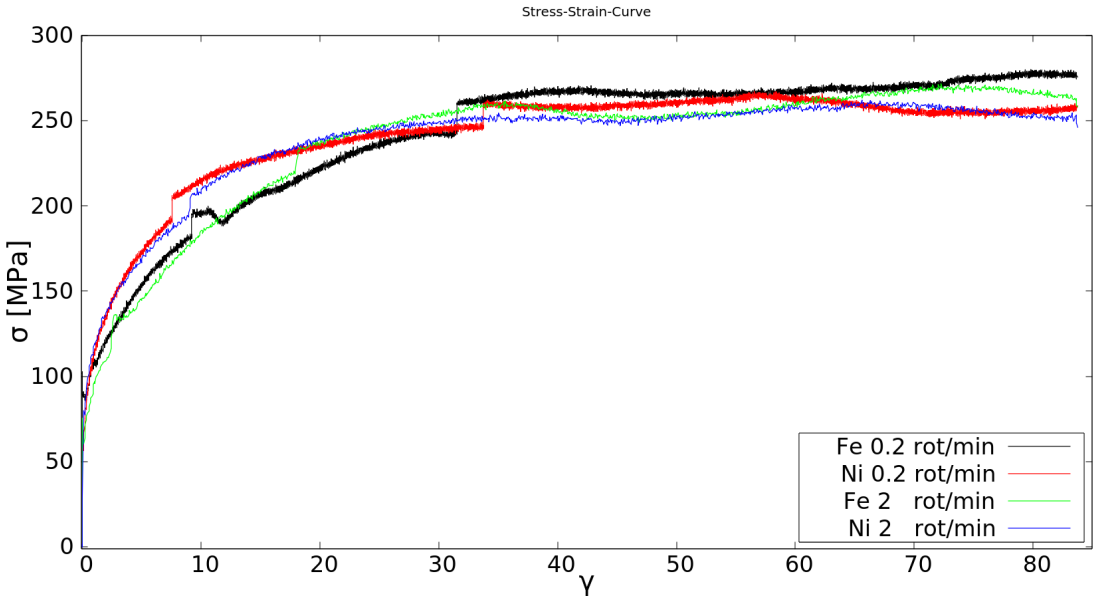

Figure 4.4: Comparison between iron and nickel stress-strain curves obtained with 2 rotations and 4 GPa at 2 $\frac{rot}{min}$ and 0.2 $\frac{rot}{min}$

4.2.2 Hardness measurements

After characterising the sample state directly after deformation yet still under 4 GPa of pressure by stress-strain curves, hardness measurements were taken to evaluate the stable sample state after releasing the pressure. This enables comparing both states. This comparison allowed drawing a conclusion concerning the importance of the overlying oscillations consistently seen in the iron and nickel deformations. One iron sample was measured 47 times on a ring at a radius of 4 mm with ≈0.5 mm distance between the measurement sites. The results are shown in Figure 4.5. It shows no discernable oscillation which indicates no connection between the stress oscillations during deformation

and the steady sample state after unloading.

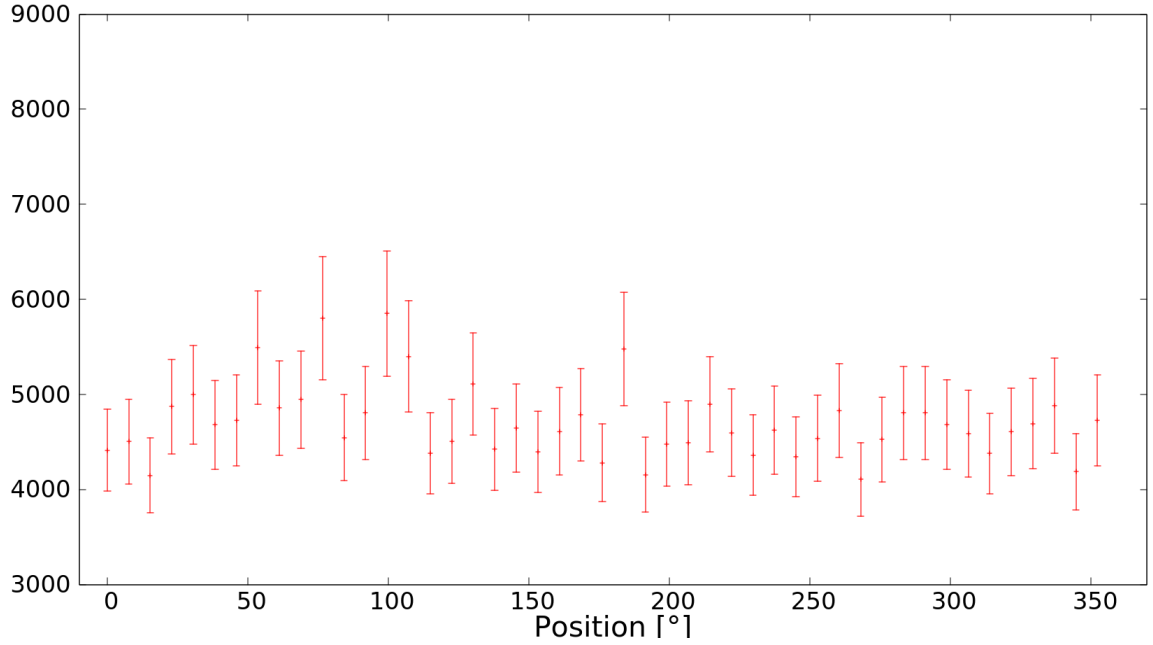

Figure 4.5: Vickers hardness measured around the edge of an iron sample deformed at 2 $\frac{rot}{min}$

4.3 Steel measurements

4.3.1 "From preliminary to main measurements"

Judging from the data displayed in Figure 4.2 and 4.3, it was concluded that the spread of two orders of magnitude is sufficient but the intervals between the speeds needed to be investigated more closely since the strain-rates in the preliminary measurements were too far apart. So in order to compare strain-rates between different rotational speeds, the parameters laid out in section 3.2.2 were chosen for the experiments conducted with Sandvik steel.

After finishing the preliminary measurements, an upgraded torque measurement tool was installed in the HPT machine in order to be able to make more accurate and less angle dependent measurements. Apart from the conversion used to attain the torque value from the raw measurement data, nothing changed in regard to this thesis.

4.3.2 Stress-strain curves

The first step for evaluating the repeated steel measurements was to check the stress-strain curves for consistency. In Figure 4.6, five stress-strain curves measured at a rotational speed of 1 $\frac{rot}{min}$ are shown. Apart from curve #3, they show good consistency, jump artefacts not withstanding. There still is a noticeable oscillation in the saturation region, most distinctly shown in curve #4, however the scale compared to the preliminary measurements is significantly smaller and will not be considered relevant in the further course of the analysis (see section 4.2.2).

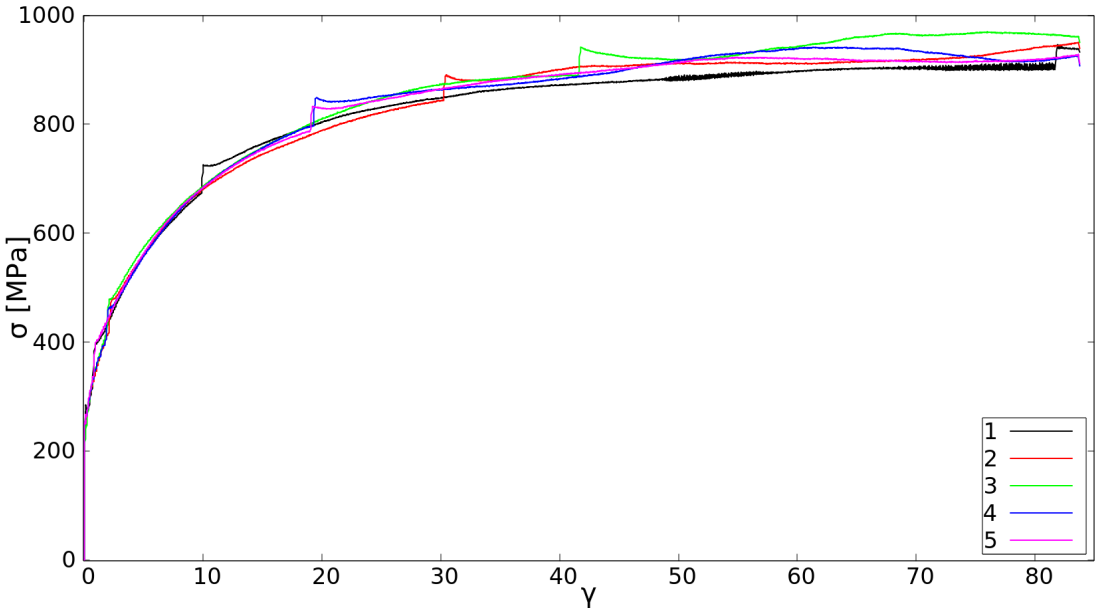

Figure 4.6: Stress-strain curves obtained from HPT deformation of Sandvik steel for 2 rotations at 4 GPa with 1 $\frac{rot}{min}$

Similarly, Figure 4.7 shows the stress-strain curves of the deformations with 0.01 $\frac{rot}{min}$, 0.06 $\frac{rot}{min}$, 0.1 $\frac{rot}{min}$ and 0.6 $\frac{rot}{min}$. Apart from curve #2 with 0.01 $\frac{rot}{min}$, which at small strains differs from the rest, all curves show the familiar run of the deformation process with jump artefacts and oscillation in the saturation range. This allows using the similar curves as basis for fitting the saturation curves explained in section 3.3.2 for further analysis.

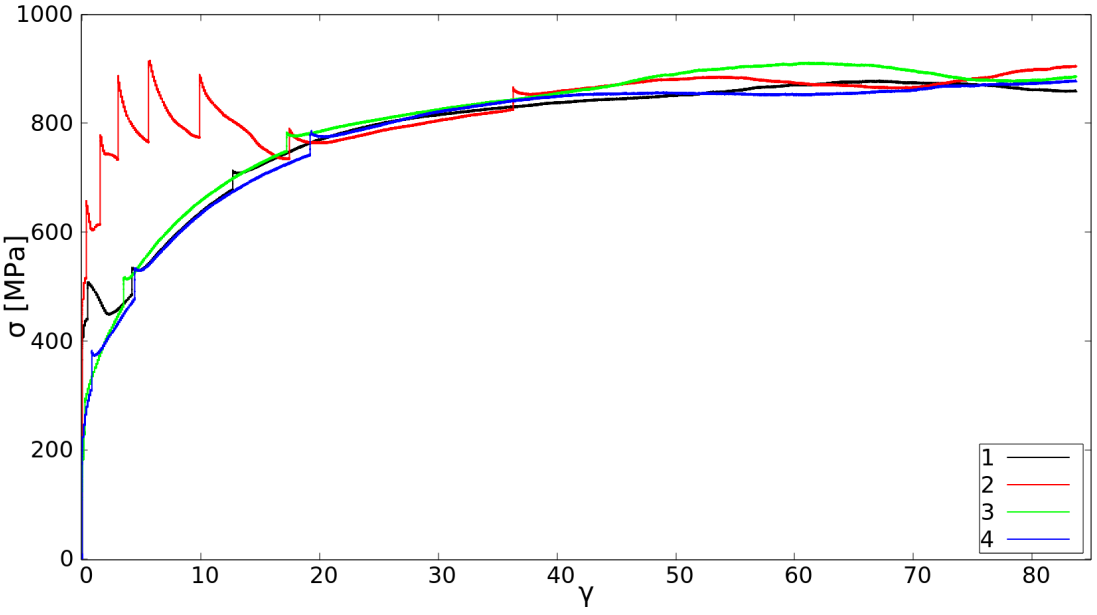
1000
800
600
400
200
0
σ [MPa]
0
10
20
30
40
50
60
70
80
γ
1
2
3
4

(a)

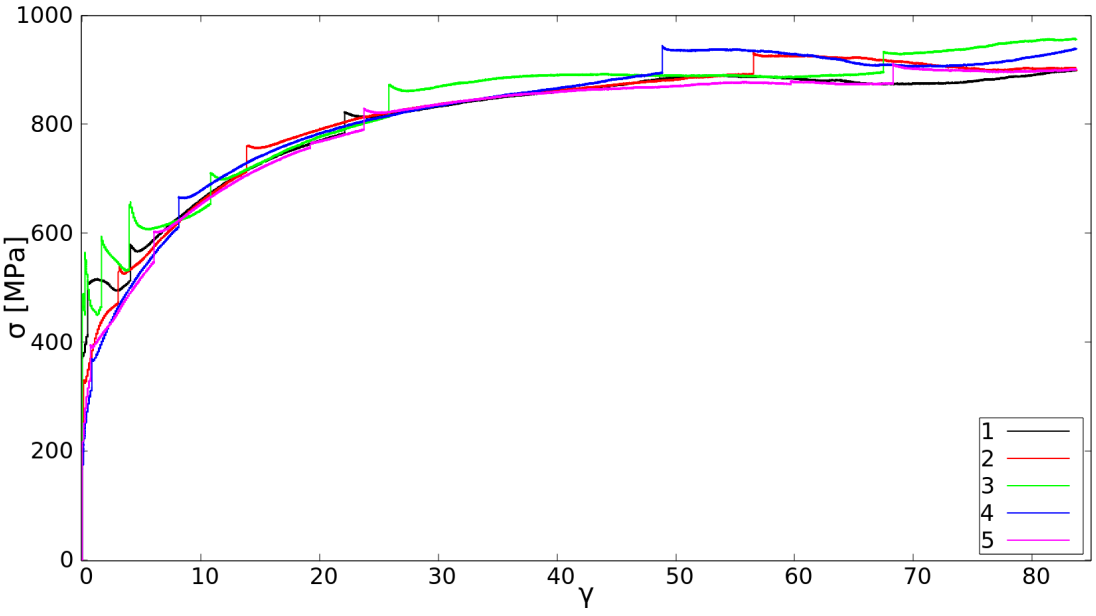
1000
800
600
400
200
0
σ [MPa]
0
10
20
30
40
50
60
70
80
γ
1
2
3
4
5

(b)

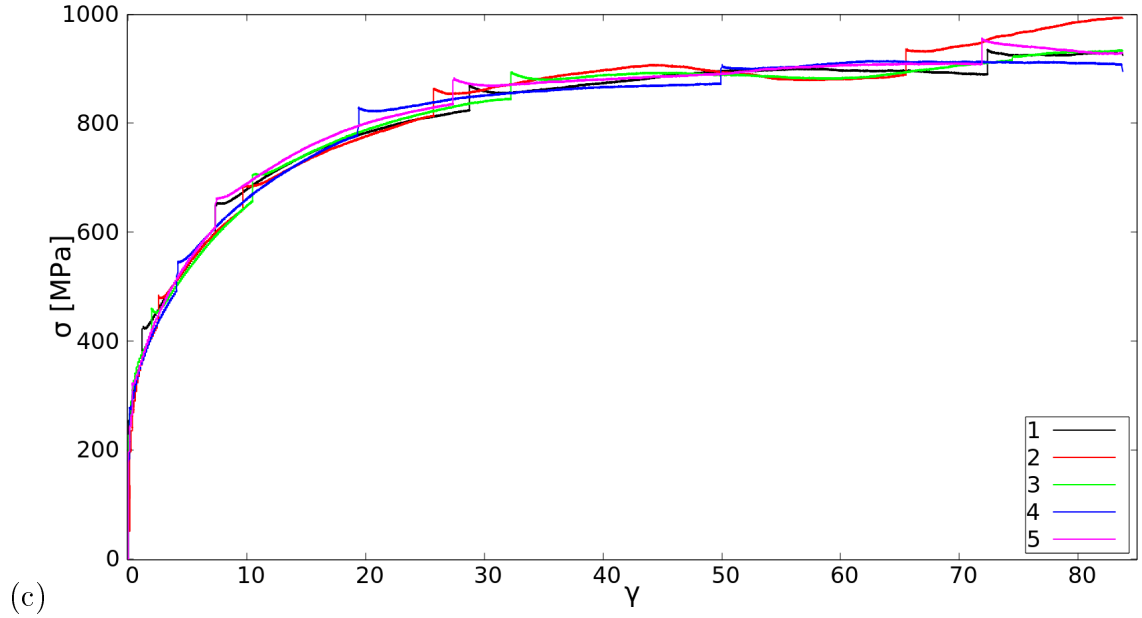

(c)

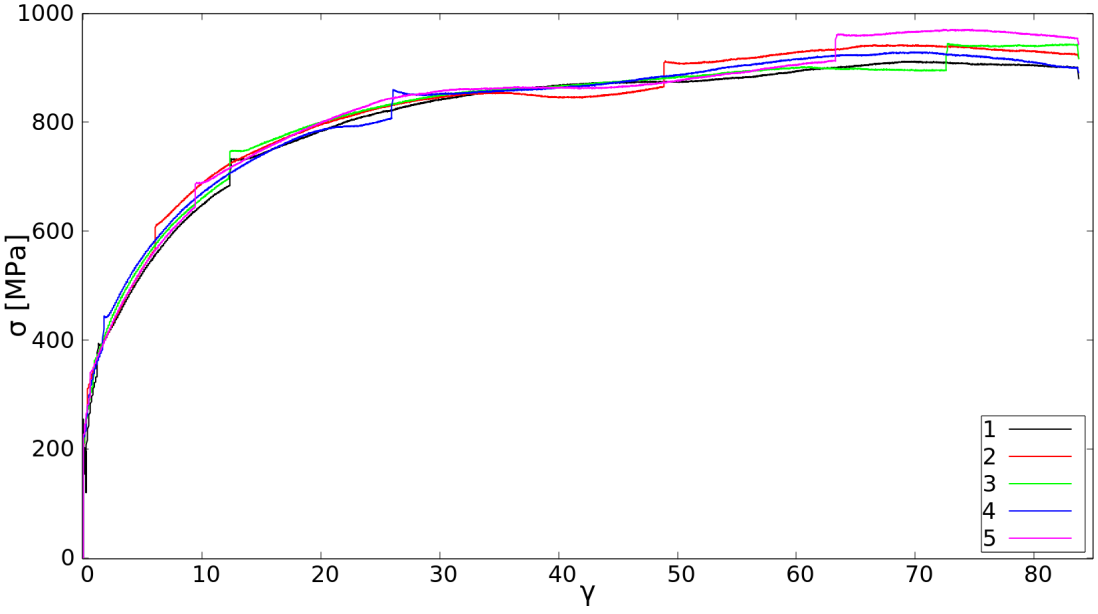

(d)

Figure 4.7: Stress-strain curves obtained from HPT deformation of Sandvik steel for 2 rotations at 4 GPa with (a) 0.01 $\frac{rot}{min}$, (b) 0.06 $\frac{rot}{min}$, (c) 0.1 $\frac{rot}{min}$, (d) 0.6 $\frac{rot}{min}$

Figure 4.8 shows the stress-strain curves recorded at 6 $\frac{rot}{min}$. While the first two deformations show similar curves that correspond with the run expected from the curves recorded at other rotational speeds, the others deviate. The general form is still that of a saturation curve, but the onset as well as the saturation level are noticeably different. They are steeper and higher respectively. Since these fast deformations took 20 seconds each, they were done in quick succession. A possible reason for the discrepancies between the first two measurements and the later ones lies in the time-frame which is significantly shorter than that of other deformation speeds. They notably only show up to two jump artefacts which means that little or no material flowed from the deformation chamber. This results in higher pressure which in turn leads to higher torque and stress values. Furthermore the higher pressure might have increased the wear on the anvils, making the edges of the anvil recess less and less defined with every deformation. This assumption is supported by the last deformation having a saturation level closer to the first two deformations while showing two jump artifacts. Less defined edges would result in higher friction, increasing the torque values. Worn edges would also allow material to flow out of the chamber even during the short deformation time, but not enough to be in an equilibrium state at the end of deformation. For these deformations, the minimal differences in sample height prior to deformation might have had an influence. Unfortunately their height was not individually traceable due to the indistinguishability of the samples prior to deformation.

The arithmetic mean of the saturation stress values obtained from the fits are displayed in table 4.2 along with their uncertainties. These uncertainties were taken as weighted mean uncertainties. Each individual uncertainty and as a result the uncertainties in table 4.2 are very small. Especially since there are systematic errors in the measurements that supersede the statistical uncertainties in table 4.2.

Rotation speed $\left[\frac{rot}{min}\right]$	Saturation stress $[MPa]$
0.01	870.1 ± 0.02
0.06	898.04 ± 0.07
0.1	906.88 ± 0.09
0.6	904.51 ± 0.27
1	913.41 ± 0.34
6	893.7 ± 1.4

Table 4.2: Mean saturation stress values of Sandvik steel from saturation fits at their respective deformation speeds

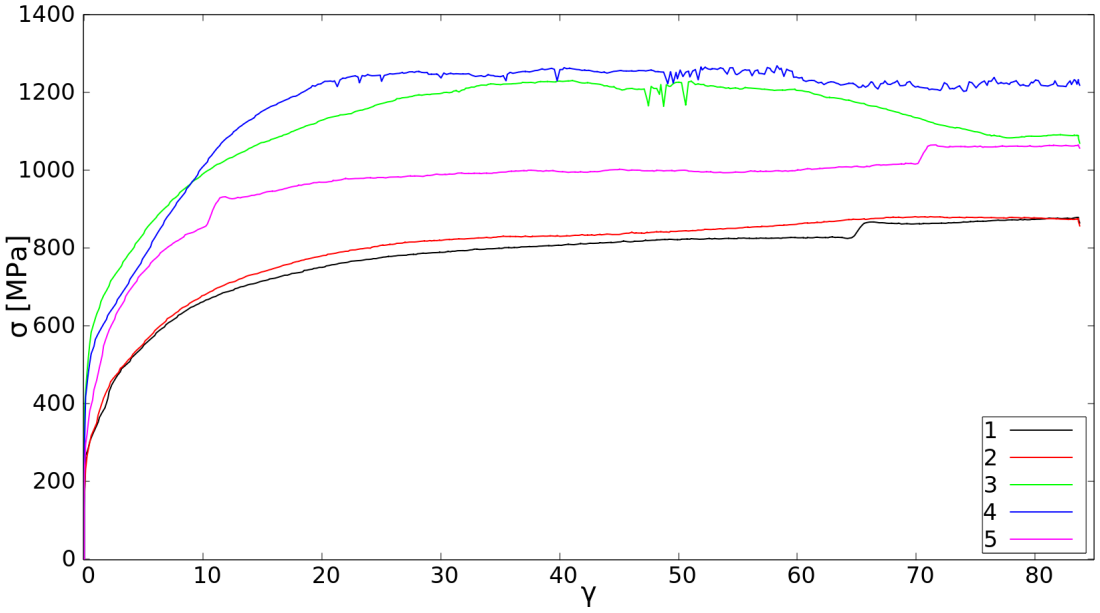

Figure 4.8: Stress-strain curves obtained from HPT deformation of Sandvik steel for 2 rotations at 4 GPa with 6 $\frac{rot}{min}$

The data set in table 4.2 with the uncertainties in equation 3.6 form the baseline to which the following data will be compared.

4.3.3 Hardness measurements

In order to compare the steady state of the samples under pressure with the steady state after relieving the pressure, the saturation stress values were compared to the respective Vickers hardness. Using at least ten indentations to calculate the mean value and the associated uncertainty, the values in table 4.3 were obtained.

Rotation speed $\left[\frac{rot}{min}\right]$	Vickers hardness $[MPa]$
0.01	4730 ± 140
0.06	4830 ± 150
0.1	4790 ± 150
0.6	5040 ± 160
1	4440 ± 140
6	4050 ± 120

Table 4.3: Mean Vickers hardness of Sandvik steel obtained from measurements on a ring with $r = 3.8\,mm$ at their respective deformation speeds

The measurements forming the basis of table 4.3 were done along a ring with the radius

of 3.8 mm so as to definitely be in a region of stress saturation.

To be able to graphically compare table 4.2 and table 4.3, both were plotted alongside each other in Figure 4.9. Graphically comparing the courses of both curves shows a vague trend both have in common. Both seem to first increase with increasing strain-rate and reach a maximum before falling off again.

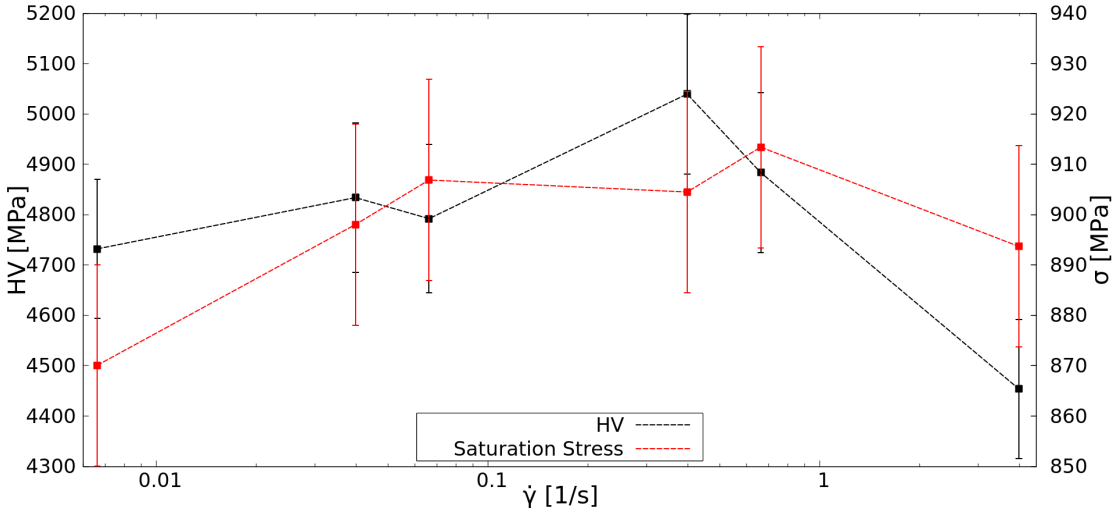

Figure 4.9: Vickers hardness at $r = 3.8\ mm$ and saturation stress of Sandvik steel plotted versus the strain-rate

Furthermore, hardness measurements were conducted at different radii in order to compare between rotation speeds and thereby examining the strain-rate dependence of the steady state after pressure release. To that end at least ten measurements were done at the radii 0.63 mm, 2 mm, 3.25 mm and 3.8 mm on one sample of each deformation speed as was elaborated in section 3.3.4. Averaging the measurements of each ring gave four hardness values for each deformation speed and six hardness values for each strain (radius), as depicted in Figure 4.10.

Clearly, the three curves corresponding to the larger strains show similar values and are therefore assumed to be in the saturation area of the samples. In contrast to that, the innermost measurements display much smaller Vickers hardness. All four curves however show a similar tendency of slightly increasing with the strain-rate and falling off at higher strain-rates. At higher strain values, the drop-off seems to occur at higher strain-rates. This is further evidence that the strain-rate does have an impact on the steady state after SPD since it confirms the findings in Figure 4.9. In this set-up, there seems to be an optimum strain-rate at which to deform in order to obtain the

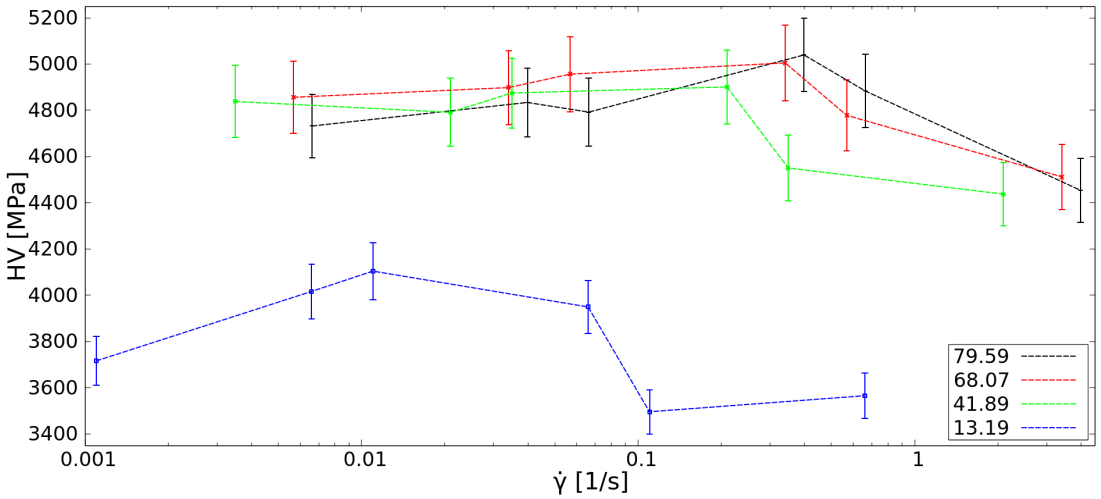

Figure 4.10: Vickers hardness values from one Sandvik steel sample of every deformation speed at four radii each plotted versus strain-rate; each radius is shown as a constant strain

maximum hardness.

4.3.4 DSC measurements

The investigation by DSC yielded the exothermic peaks of annealing the defects in the sample. An example measurement is shown in Figure 3.5, the obtained data is shown in table 4.4.

The first peaks lie in the range from 150°C to 210°C signifying the annealing of single vacancies [7].

Rotation speed $\left[\frac{rot}{min}\right]$	Peak temperature [°C]	Peak area $\left[\frac{J}{g}\right]$
0.01	314 ± 3	1.27 ± 0.05
0.06	290 ± 3	1.25 ± 0.05
0.1	288 ± 3	0.9 ± 0.05
0.6	294 ± 3	0.66 ± 0.05
1	296 ± 3	0.97 ± 0.05
6	310 ± 3	1.15 ± 0.05

Table 4.4: Peak temperatures and peak areas obtained from DSC measurements of Sandvik steel at their respective deformation speeds

Figure 4.11 shows the peak temperatures and the calculated stored energy versus their respective strain rates. According to the findings of [14], approximately 25% of the

stored energy can be attributed to vacancy agglomerates annealing. The course of the graphs shows an opposite trend to Figure 4.9 and 4.10 as the curves decline to a minimum and then increase again almost reaching the level of the lower strain-rates. The low values of stored energy suggest lower inner tension in the deformed sample. That could stem from either a more ordered arrangement of dislocations or from a higher ratio of vacancy agglomerates. Both would lower the inner tension due to fewer interlocked dislocations.

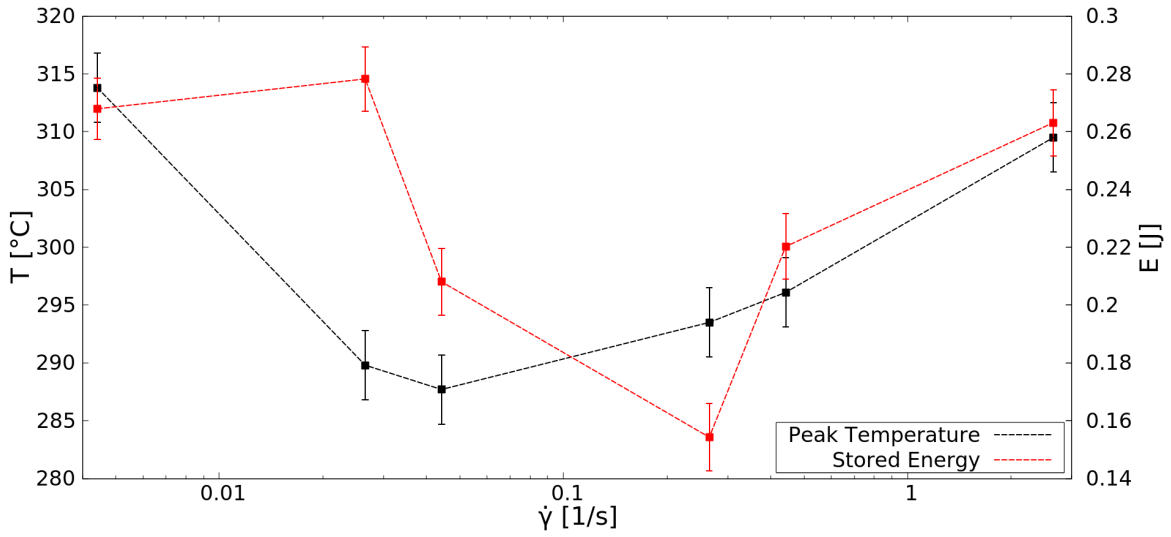

Figure 4.11: Peak temperatures and calculated stored energy of Sandvik steel plotted versus strain-rate

Since this seems counter-intuitive, it would be interesting to further investigate in order to ascertain the nature of the dislocation configuration in the samples. This might give more insight into the process of dislocation storage at very low and very high strain-rates. One has to keep in mind that DSC is an indirect method of analysis and thus demands caution when interpreting the single measurements conducted in the scope of this thesis. To attain more reliable data, more DSC measurements could be done in the future.

A possible explanation for the behaviour shown in Figure 4.11 is the positioning of the dislocations in relation to each other. High dislocation density with few intersections could be the cause for low hardness values and vice versa. Further investigation with X-ray analysis could give insight into the composition of the dislocations. This however

is not expected to actually cause the dislocation density to be cut in half as is shown in Figure 4.11.

Another possible explanation is the formation of grain boundaries at specific strain-rates. Usually their annealing would be expected to show in the DSC measurements. This again could be investigated further by X-ray diffraction and DSC measurements.

4.3.5 Strain-rate sensitivity

After implicitly analysing the strain-rate sensitivity of Sandvik steel, equation 2.3 was used with the saturation stress values from Figure 4.9 in order to visualise the strain-rate sensitivity in Figure 4.12. The values do not suggest a linear relation but rather an increase at first, a stagnation in the range $-1 \leq \ln(\dot{\gamma}) \leq 0$ and a decrease after that. Building on that, a polynomial of the form

$$f(x) = ax^2 + bx + c \tag{4.2}$$

Fit Parameter	Fit Value
a	-0.003 ± 0.0005
b	-0.007 ± 0.002
c	6.81 ± 0.003

Table 4.5: Fit-parameters of the curve shown in Figure 4.12

was fitted to the data. The resulting curve is shown in Figure 4.12. The fit parameters are displayed in table 4.5.

Figure 4.12 suggests a shift in the equilibrium between generation and annihilation of dislocations in favour of annihilation with increasing strain rate. One reason could be adiabatic heating which would anneal very small volumes of the sample during deformation and therefore reduce the overall dislocation density.

This is in contrast to the assumption that SRS is constant at high strain-rates but rather indicates that it decreases further at high strain-rates. Further investigation with even finer intervals of strain-rate and therefore more data points along a possible curve would verify or disprove this thesis.

To illustrate the evolution of the SRS with respect to the strain-rate, Figure 4.13 shows SRS values based on the fitted curve from Figure 4.12. Comparing Figure 4.13 with

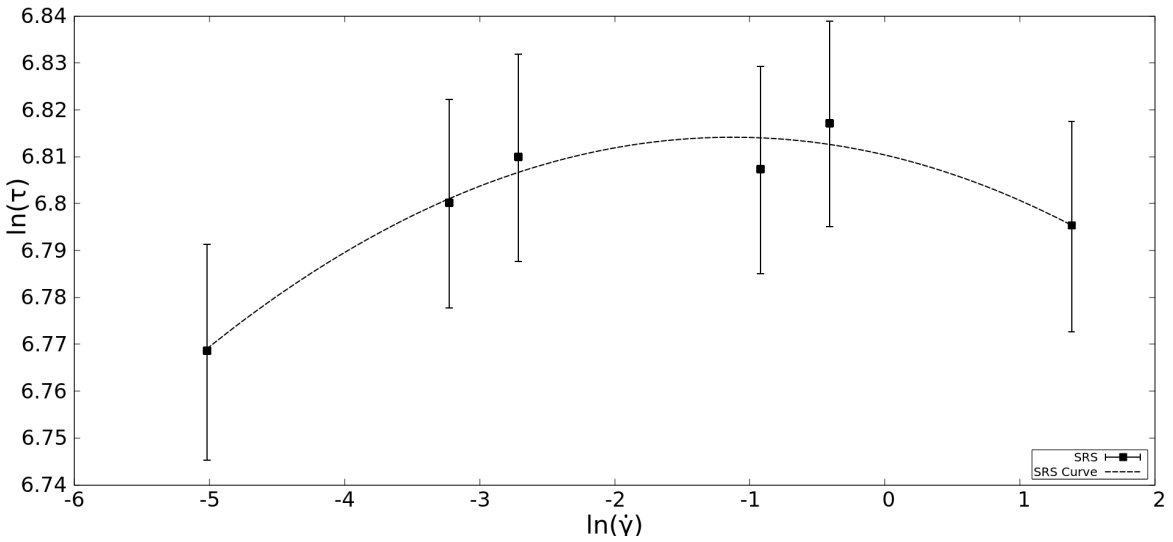

Figure 4.12: Logarithms of steady state stress and strain-rate plotted versus each other visualising the SRS according to equation 2.3

results from [20] shows a very nice correspondence in the course of the SRS, although the material used was copper instead of Sandvik steel and the data were acquired by tensile testing on ECAP-deformed samples rather than in-situ measurements with HPT.

Existing works on the SRS of steels using tensile tests [1,3] show a similar yield strength trend: "shallow at low rates, and ever steeper with increasing strain-rate." [3]. This trend nicely ties into the description of the work hardening stages in [12] discussed in chapter 2.2. Putting both in perspective to each other places the results from [1] and [3] in stage I transitioning into stage II.

Excluding stage III, [22, 24] elaborate on the SRS in stages IV and V. Especially [24] shows the SRS parameter m increasing with increasing stress in two steps. While the SRS develops similarly with different temperatures, the development with increasing stress stays the same.

Considering mainly these papers, but also [9, 23], the results depicted in Figure 4.12 should be extended by similar measurements at different temperatures, expecting lower SRS at lower temperatures and higher SRS at higher temperatures [9, 24].

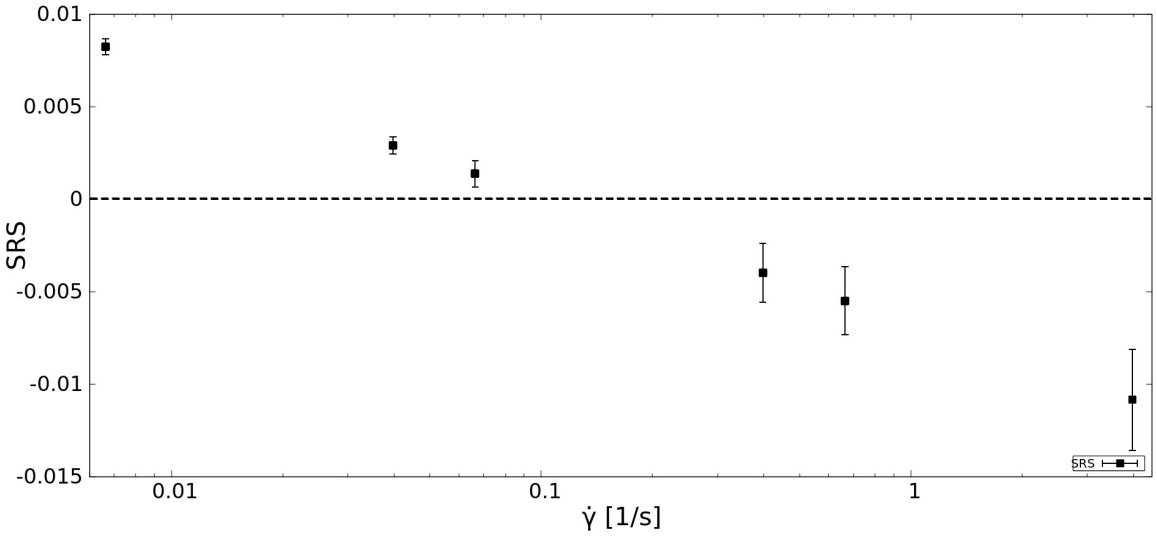

Figure 4.13: SRS values derived from polynomial fit plotted versus strain-rate

Chapter 5

Summary and Conclusion

The strain-rate sensitivity of Sandvik Bioline 316LVM austenitic stainless steel was investigated at high strains applied by HPT.

The in-situ stress measurements were compared to Vickers hardness measurements, each with respect to strain-rate. Their comparison did not yield a conclusive hint towards a strain-rate dependent change between the steady state under pressure and the steady state after release. Both series of values however congruently show an increase with strain-rate to a peak around $\dot{\gamma} = 0.5\ \frac{1}{s}$ and fall off again at higher strain-rates. These results are consistent within the assumed uncertainties and therefore strongly indicate a changing strain-rate sensitivity with strain-rate.

To further investigate the impact of the strain-rate on the dislocations as the main contributing factor to work hardening at high strains, DSC measurements were conducted. Contrary to expectations induced by the measurements mentioned above, the dislocation density as well as the peak temperature show an inverse behaviour by decreasing with strain-rate down to a minimum and rising again at high strain-rates. Not withstanding several attempts, the inverse behaviour could not be conclusively explained in the scope of this thesis. Verifying the data and developing a sound explanation poses an interesting challenge for future research.

All in all the experiments conducted strongly suggest not only a change in strain-rate sensitivity with changing strain-rate but even a change in the sign of the strain-rate sensitivity at very high strain-rates.

Since this was done at room temperature, only assumptions can be made on the be-

haviour at extreme temperatures. At high temperatures, the higher dislocation mobility should lead to less dislocation storage, less saturation stress and therefore less work hardening. Vice versa, low temperature deformations should lead to higher work hardening due to more static dislocations which are stored more frequently. It is however very possible that such samples would not retain their high stress levels at room temperature.

Studies have shown that SRS increases with temperature at lower stress values. Investigating the strain-rate sensitivity of highly deformed metals at extreme temperatures would extend the results of this thesis.

Bibliography

[1] W. Bleck and I. Schael. Determination of crash-relevant material parameters by dynamic tensile tests. *Steel Research*, 71(5):171–173, 2000.

[2] E.V. Boltynjuk, D.V. Gunderov, E.V. Ubyivovk, M.A. Monclús, L.W. Yang, J.M. Molina-Aldareguia, A.I. Tyurin, A.R. Kilmametov, A.A. Churakova, A.Yu. Churyumov, and R.Z. Valiev. Enhanced strain rate sensitivity of zr-based bulk metallic glasses subjected to high pressure torsion. *Journal of Alloys and Compounds*, 747:595–602, 2018.

[3] B.L. Boyce and M.F. Dilmore. The dynamic tensile behavior of tough, ultrahigh-strength steels at strain-rates from 0.0002 to 200. *International Journal of Impact Engineering*, 36:263–271, 2009.

[4] Setman D. *Lattice defects in HPT processed fcc nanometals studied by differential scanning calorimetry.* PhD thesis, University of vienna, 2010.

[5] A.K. Ghosh. On the measurement of strain rate sensitivity for deformation mechanism in conventional and ultra-fine grain alloys. *Materials Science and Engineering A 463 36-40*, 2007.

[6] Günter Gottstein. *Materialwissenschaft und Werkstofftechnik.* Springer Vieweg, 2014.

[7] Sheraz Khakwani. *Bulk Nanocrystalline Soft Magnetic Fe-Si-X Alloys Achieved Through Severe Plastic Deformation.* PhD thesis, University of Vienna, 2019.

[8] Agnieszka T. Krawczynska, Stanislaw Gierlotka, Przemyslaw Suchecki, Daria Setman, Boguslawa Adamczyk-Cieslak, Michal Gloc, Witold Chrominski, Malgorzata Lewandowska, and Michael Zehetbauer. Phenomena occurring in nanostructured

stainless steel 316lvm during annealing under high hydrostatic pressure. *Adv. Eng. Mater.*, 21(1800101), 2019.

[9] P. Les, H.P. Stuewe, and M.J. Zehetbauer. Hardening and strain rate sensitivity in stage iv of deformation in f.c.c. and b.c.c. metals. *Materials Science and Engineering A234-236 453-455*, 1997.

[10] Bönisch M., Zehetbauer M.J., Krystian M., Setman D., and Krexner G. Stabilization of lattice defects in hpt-deformed palladium hydride. *Mater. Sci. Forum*, pages 427–432, 2011.

[11] Krystian M., Setman D., Mingler B., Krexner G., and Zehetbauer M.J. Formation of superabundant vacancies in nano-pd-h generated by high-pressure torsion. *Scripta Materialia*, 62(1):49–52, 2010.

[12] A.D. Rollett and U.F. Kocks. A review of the stages of work hardening. *Solid State Phenomena*, 35-36:1–18, 1993.

[13] Erhard Schafler. *Investigation of highly deformed metals by means of X-ray Bragg-peak profile analysis*. PhD thesis, University of Vienna, 1998.

[14] Daria Setman, Erhard Schafler, Elena Korznikova, and M.J. Zehetbauer. The presence and nature of vacancy type defects in nanometals detained by severe plastic deformation. *Materials Science and Engineering*, (493):116–122, 2008.

[15] R.Z. Valiev, I.V. Alexandrov, Y.T. Zhu, and T.C. Lowe. Paradox of strength and ductility in metals processed by severe plastic deformation. *Journal of Materials Research*, 17(1), 2002.

[16] R.Z. Valiev, Y. Estrin, Z. Horita, T.G. Langdon, M.J. Zehetbauer, and Y.T. Zhu. Producing bulk ultrafine-grained materials by severe plastic deformation. *JOM*, (58):33–39, 2006.

[17] R.Z. Valiev, R.K. Islamgaliev, and I.V. Alexandrov. Bulk nanostructured materials from severe plastic deformation. *Prog. Mater. Sci.*, 45:103–189, 2000.

[18] R.Z. Valiev and T.G. Langdon. Principles of equal-channel angular pressing as a processing tool for grain refinement. *Prog. Mater. Sci.*, 51:881–981, 2006.

[19] Y.M. Wang and E. Ma. Strain hardening, strain rate sensitivity, and ductility of nanostructured metals. *Materials Science and Engineering*, 2004.

[20] Y.M. Wang and E. Ma. Three strategies to achieve uniform tensile deformation in a nanostructured metal. *Acta Materialia*, 52:1699–1709, 2004.

[21] Q. Wei, S. Cheng, K.T. Ramesh, and E. Ma. Effect of nanocrystalline and ultrafine grain sizes on the strain rate sensitivity and activation volume: fcc versus bcc metals. *Materials Science and Engineering*, A 381:71–79, 2004.

[22] M. Zehetbauer. Cold work hardening in stages iv and v of f.c.c. metals - ii model fits and physical results. *Acta metall. mater.*, 41(2):589–599, 1993.

[23] M. Zehetbauer and P. Les. Features and modelling of strengthening in late stages of high temperature deformation. *35th Annual Conference of Metallurgists*, pages 205–217, 1996.

[24] M. Zehetbauer and V. Seumer. Cold work hardening in stages iv and v of f.c.c. metals - i. experiments and interpretation. *Acta metall. mater.*, 41(2):577–588, 1993.

[25] M.J. Zehetbauer, H.P. Stüwe, A. Vorhauer, E. Schafler, and J. Kohout. The role of hydrostatic pressure in severe plastic deformation. *Adv. Eng. Mater.*, 5:273–283, 2003.

[26] M.J. Zehetbauer and Y.T. Zhu. *Bulk Nanostructered Materials.* WILEY VCH, Germany, 2009.

[27] Alexander P. Zhilyaev and Terence G. Langdon. Using high-pressure torsion for metal processing: Fundamentals and applications. *Progress in Materials Science*, 53:893–979, 2008.

Appendix A

Steel Deformation Fits

A.1 0.01 Rotations per Second

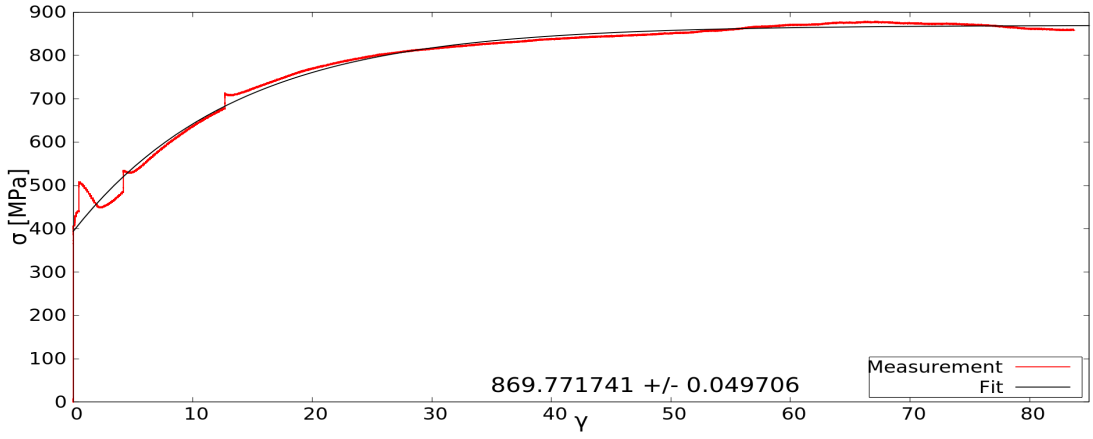

Figure A.1: Saturation curve fitted to the data from deformation # 1 at 0.01 $\frac{rot}{min}$ with the saturation stress value from the fit

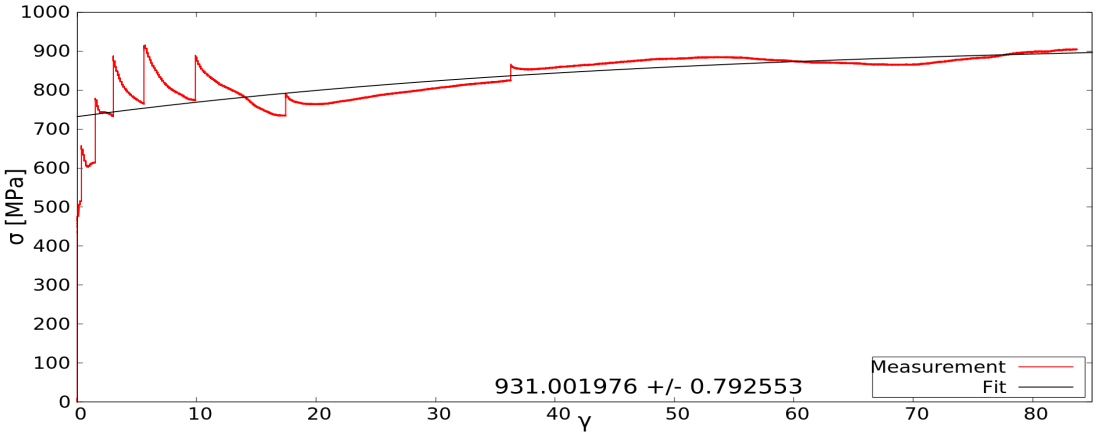

Figure A.2: Saturation curve fitted to the data from deformation # 2 at 0.01 $\frac{rot}{min}$ with the saturation stress value from the fit

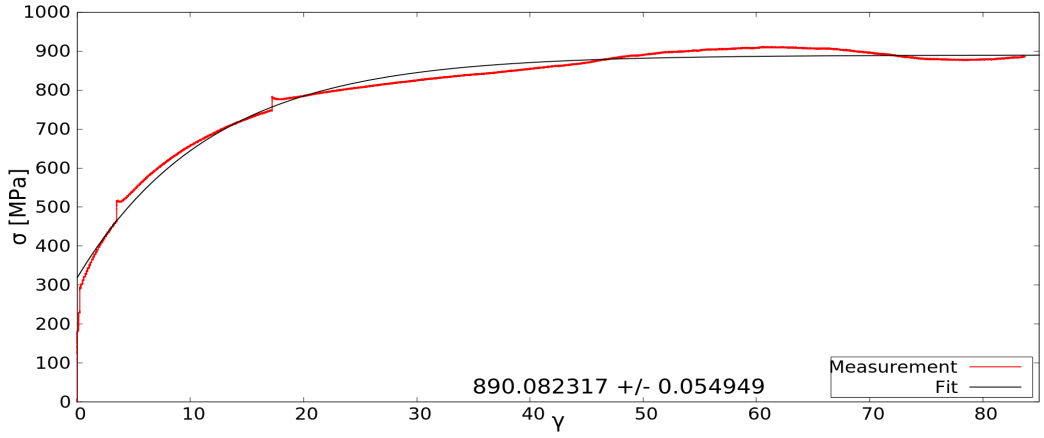

Figure A.3: Saturation curve fitted to the data from deformation # 3 at 0.01 $\frac{rot}{min}$ with the saturation stress value from the fit

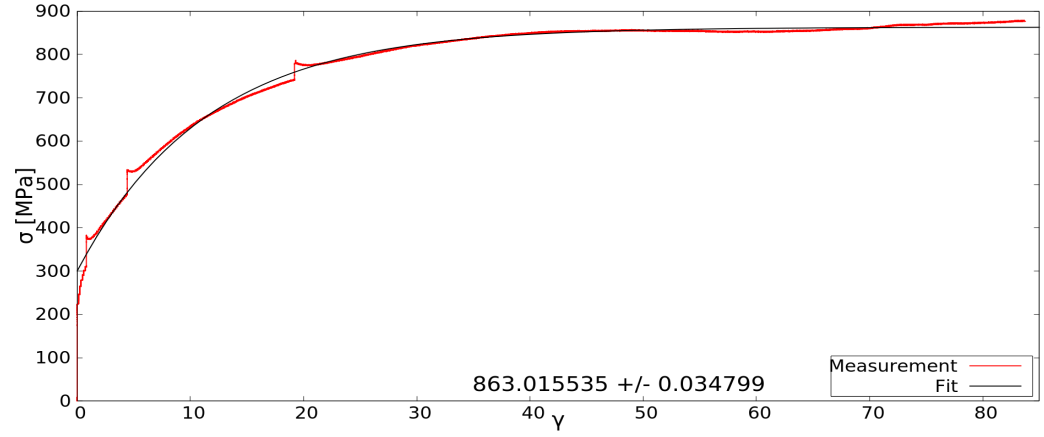

Figure A.4: Saturation curve fitted to the data from deformation # 4 at 0.01 $\frac{rot}{min}$ with the saturation stress value from the fit

A.2 0.06 Rotations per Second

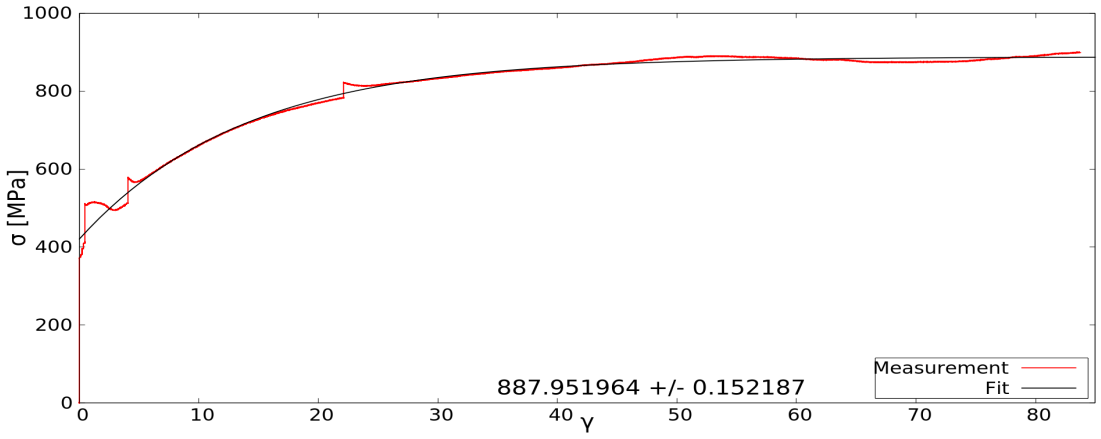

Figure A.5: Saturation curve fitted to the data from deformation # 1 at 0.06 $\frac{rot}{min}$ with the saturation stress value from the fit

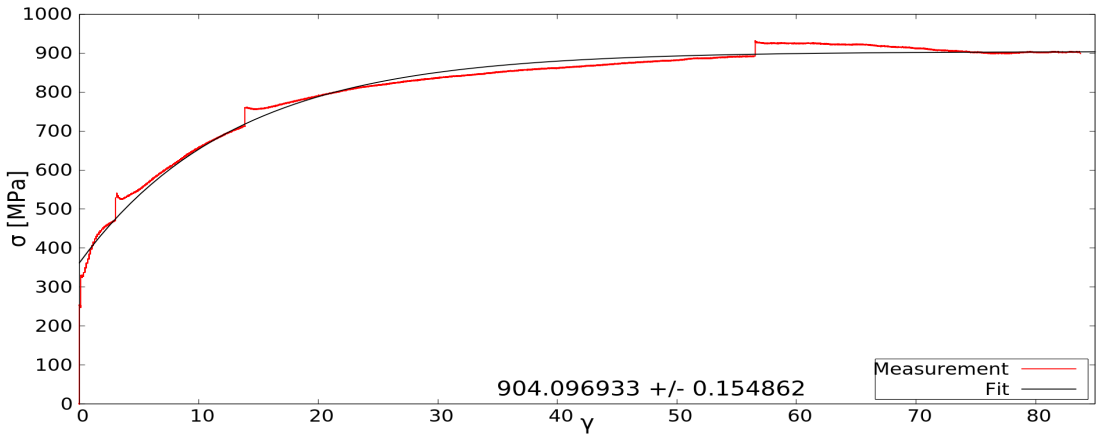

Figure A.6: Saturation curve fitted to the data from deformation # 2 at 0.06 $\frac{rot}{min}$ with the saturation stress value from the fit

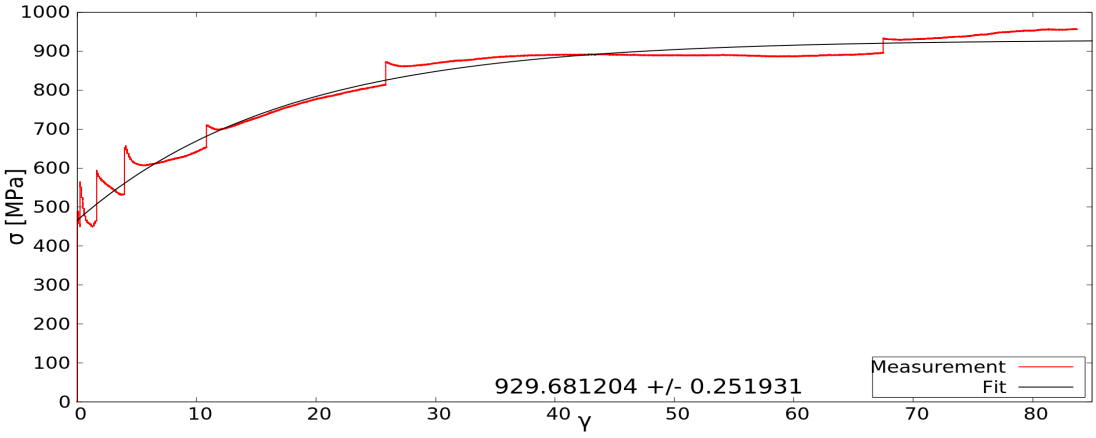

Figure A.7: Saturation curve fitted to the data from deformation # 3 at 0.06 $\frac{rot}{min}$ with the saturation stress value from the fit

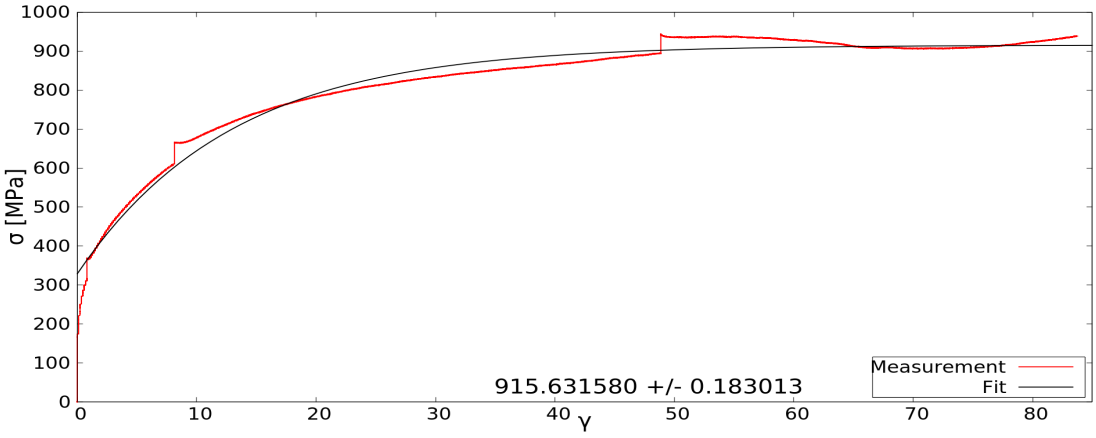

Figure A.8: Saturation curve fitted to the data from deformation # 4 at 0.06 $\frac{rot}{min}$ with the saturation stress value from the fit

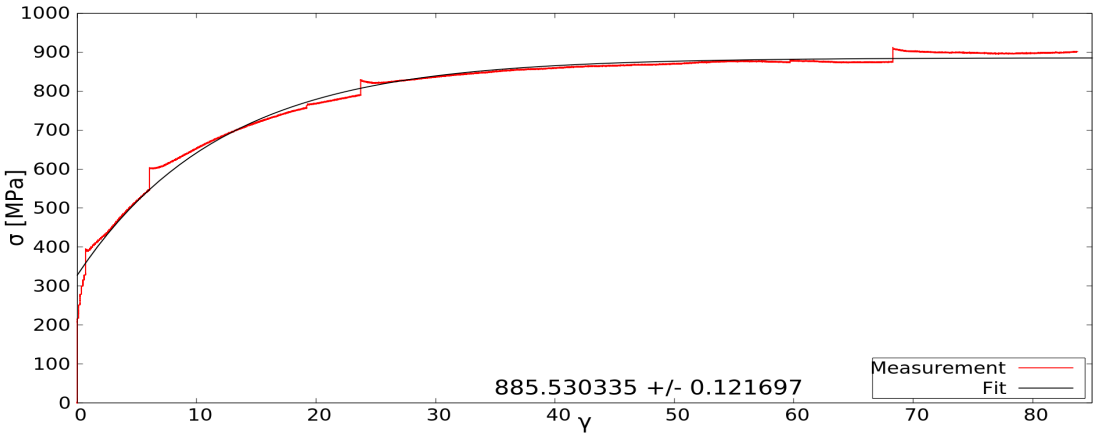

Figure A.9: Saturation curve fitted to the data from deformation # 5 at 0.06 $\frac{rot}{min}$ with the saturation stress value from the fit

A.3 0.1 Rotations per Second

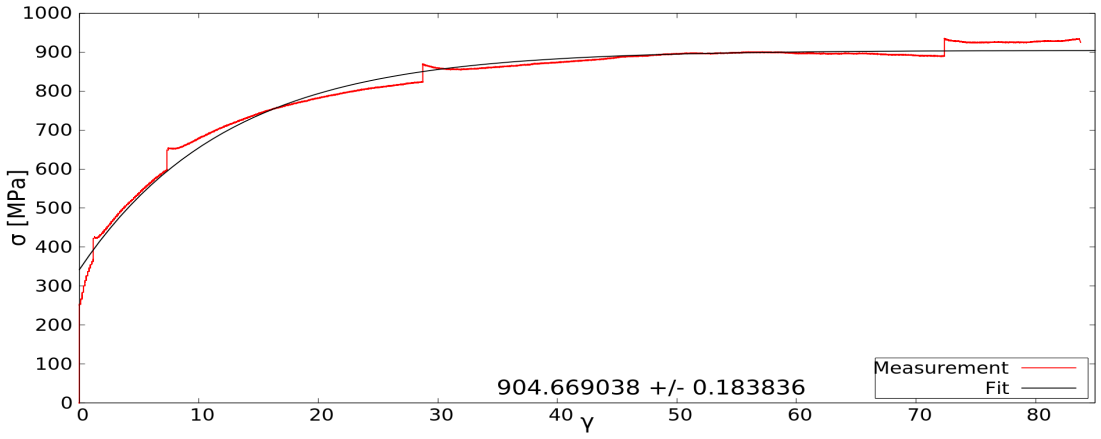

Figure A.10: Saturation curve fitted to the data from deformation # 1 at 0.1 $\frac{rot}{min}$ with the saturation stress value from the fit

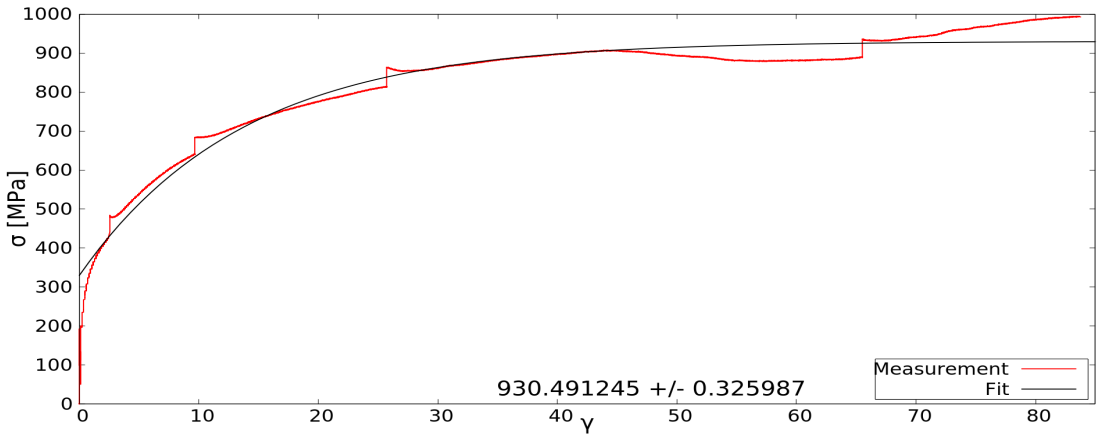

Figure A.11: Saturation curve fitted to the data from deformation # 2 at 0.1 $\frac{rot}{min}$ with the saturation stress value from the fit

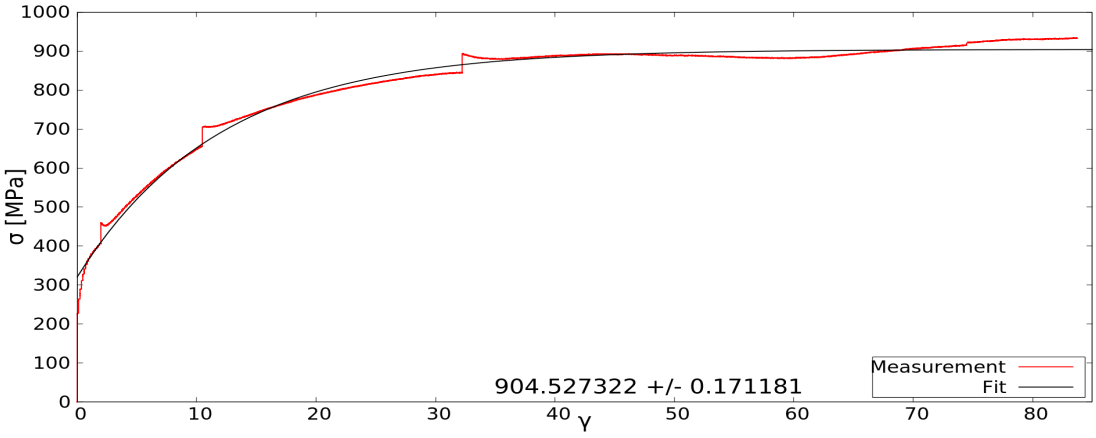

Figure A.12: Saturation curve fitted to the data from deformation # 3 at 0.1 $\frac{rot}{min}$ with the saturation stress value from the fit

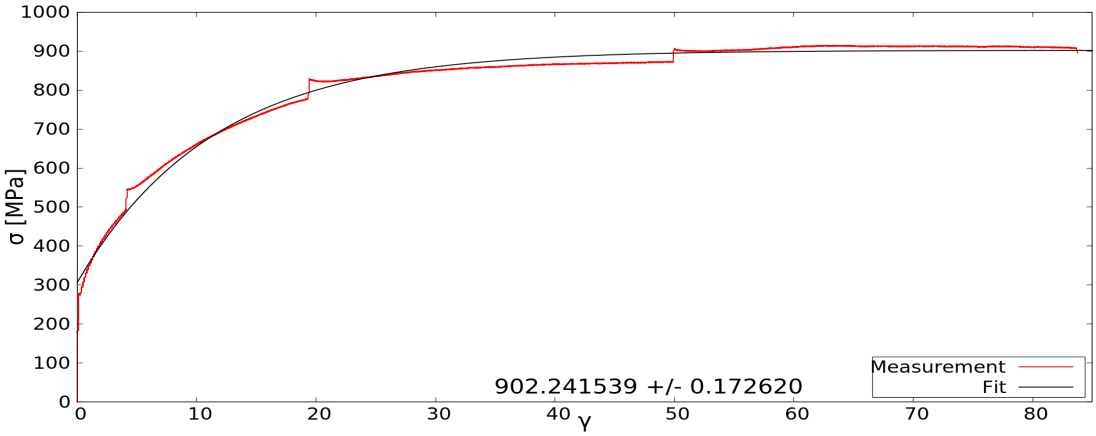

Figure A.13: Saturation curve fitted to the data from deformation # 4 at 0.1 $\frac{rot}{min}$ with the saturation stress value from the fit

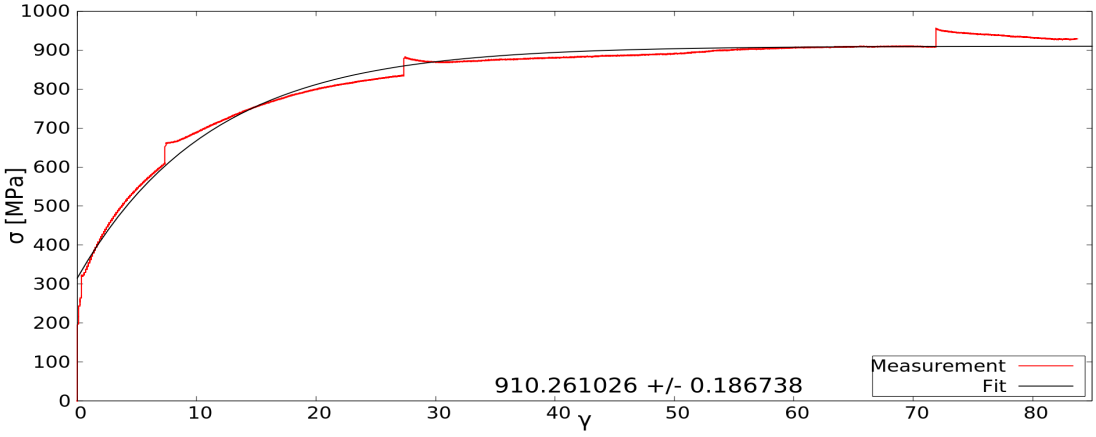

Figure A.14: Saturation curve fitted to the data from deformation # 5 at 0.1 $\frac{rot}{min}$ with the saturation stress value from the fit

A.4 0.6 Rotations per Second

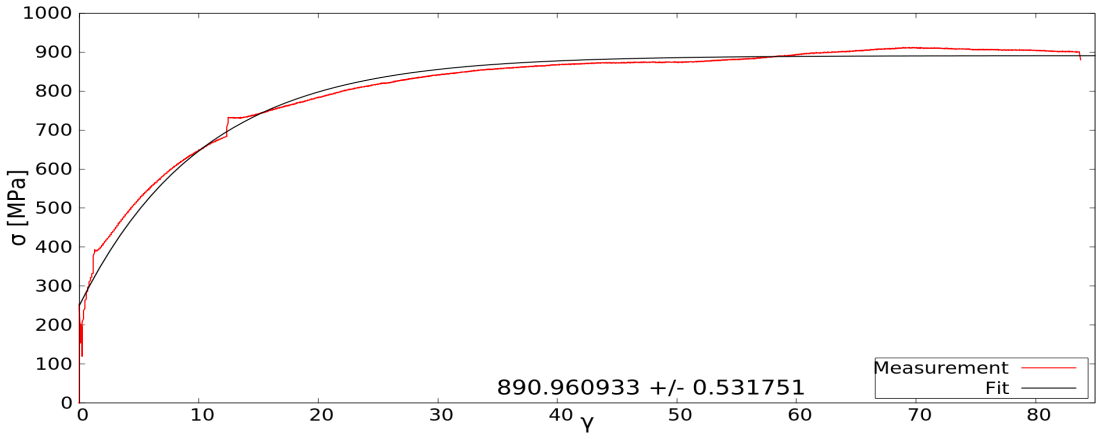

Figure A.15: Saturation curve fitted to the data from deformation # 1 at 0.6 $\frac{rot}{min}$ with the saturation stress value from the fit

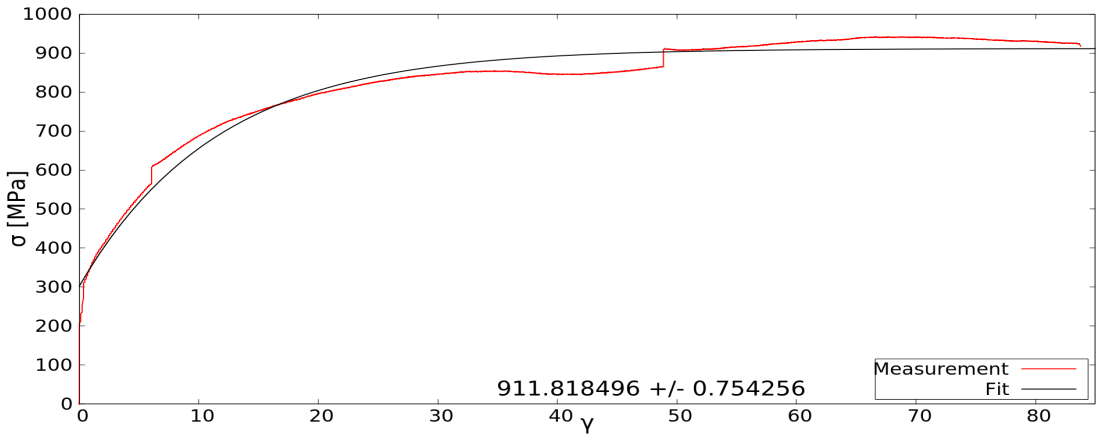

Figure A.16: Saturation curve fitted to the data from deformation # 2 at 0.6 $\frac{rot}{min}$ with the saturation stress value from the fit

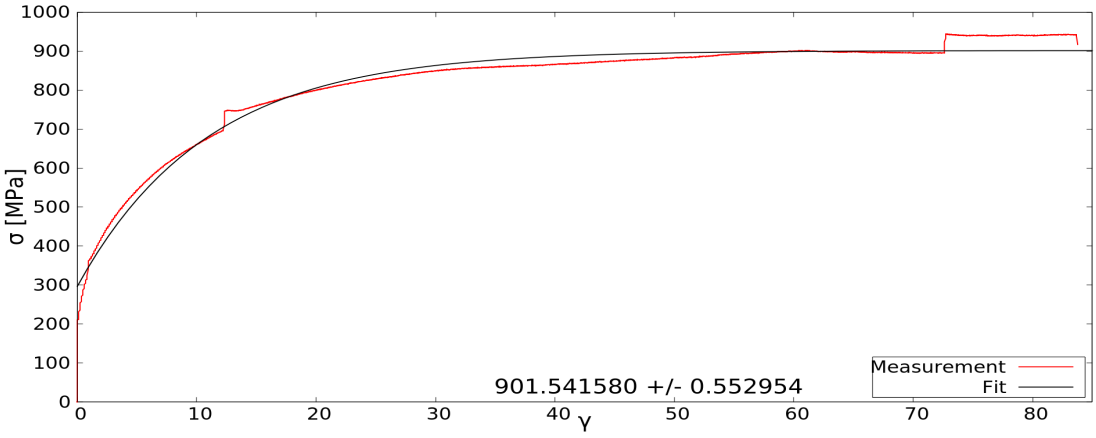

Figure A.17: Saturation curve fitted to the data from deformation # 3 at 0.6 $\frac{rot}{min}$ with the saturation stress value from the fit

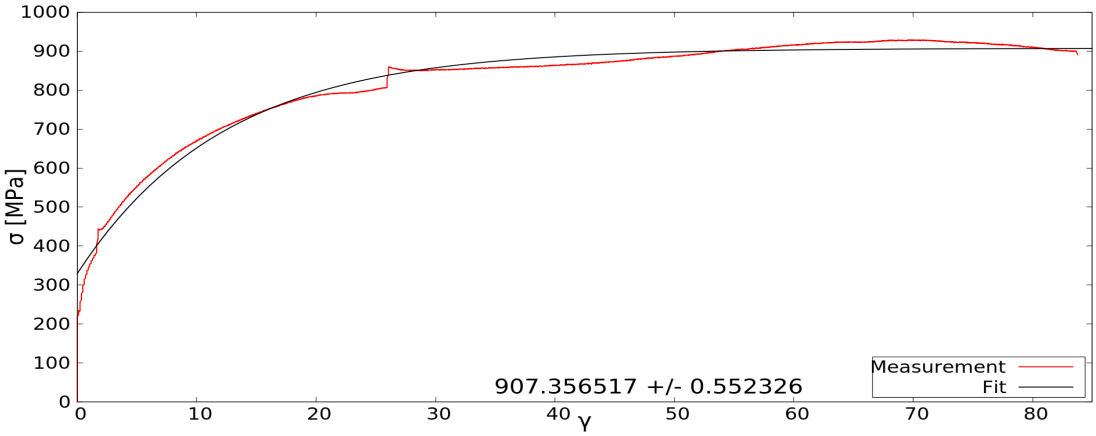

Figure A.18: Saturation curve fitted to the data from deformation # 4 at 0.6 $\frac{rot}{min}$ with the saturation stress value from the fit

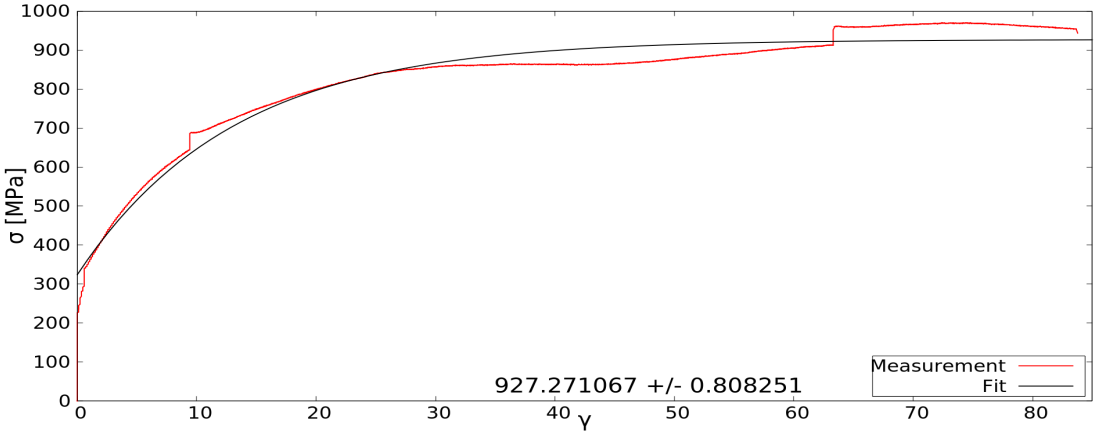

Figure A.19: Saturation curve fitted to the data from deformation # 5 at 0.6 $\frac{rot}{min}$ with the saturation stress value from the fit

A.5 1 Rotation per Second

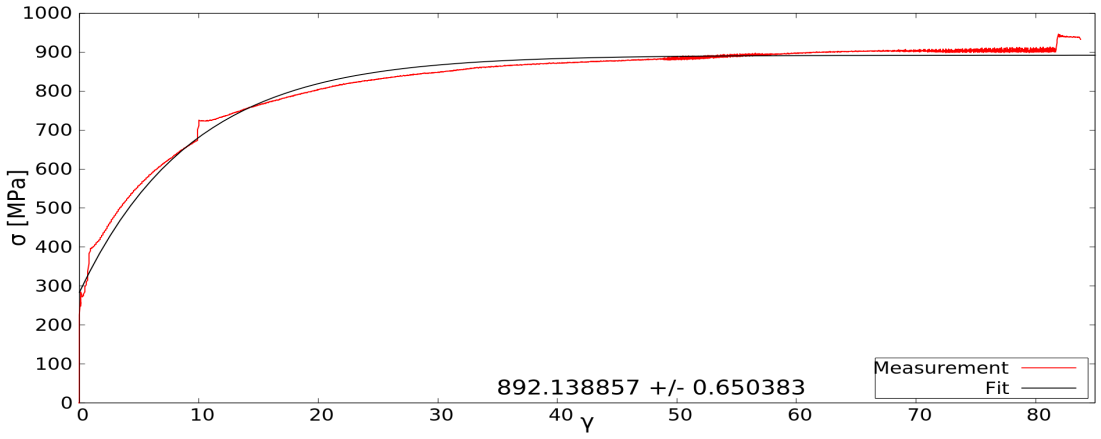

Figure A.20: Saturation curve fitted to the data from deformation # 1 at 1 $\frac{rot}{min}$ with the saturation stress value from the fit

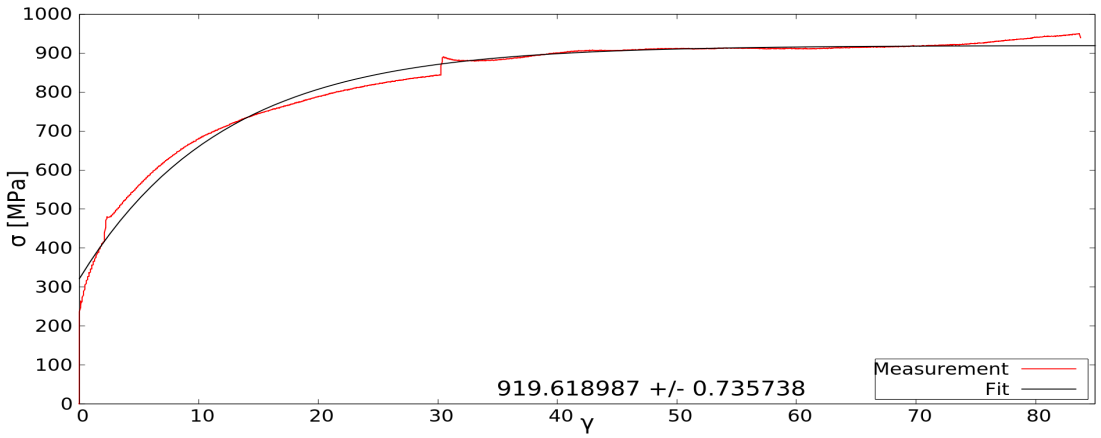

Figure A.21: Saturation curve fitted to the data from deformation # 2 at 1 $\frac{rot}{min}$ with the saturation stress value from the fit

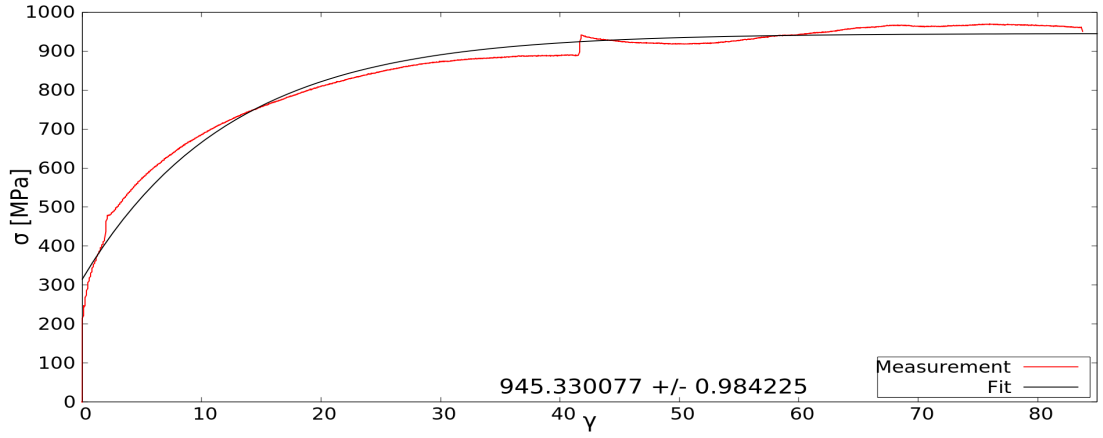

Figure A.22: Saturation curve fitted to the data from deformation # 3 at 1 $\frac{rot}{min}$ with the saturation stress value from the fit

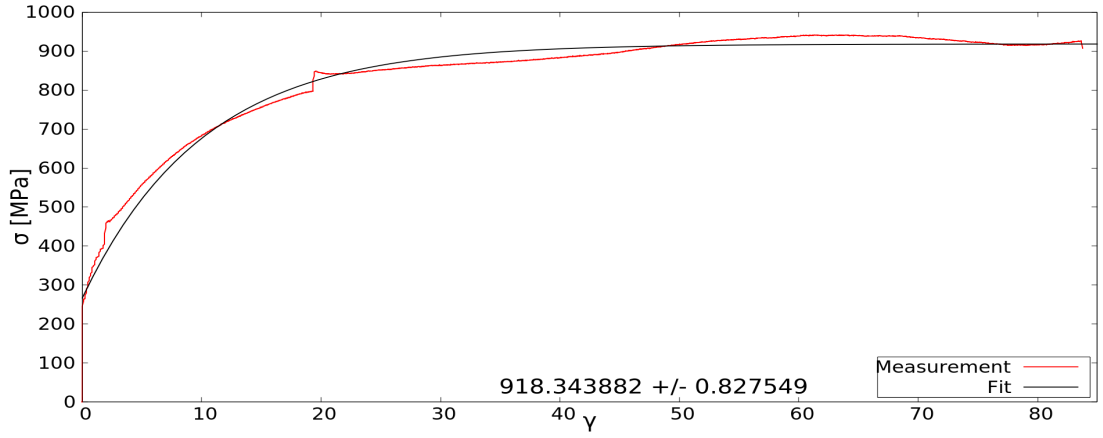

Figure A.23: Saturation curve fitted to the data from deformation # 4 at 1 $\frac{rot}{min}$ with the saturation stress value from the fit

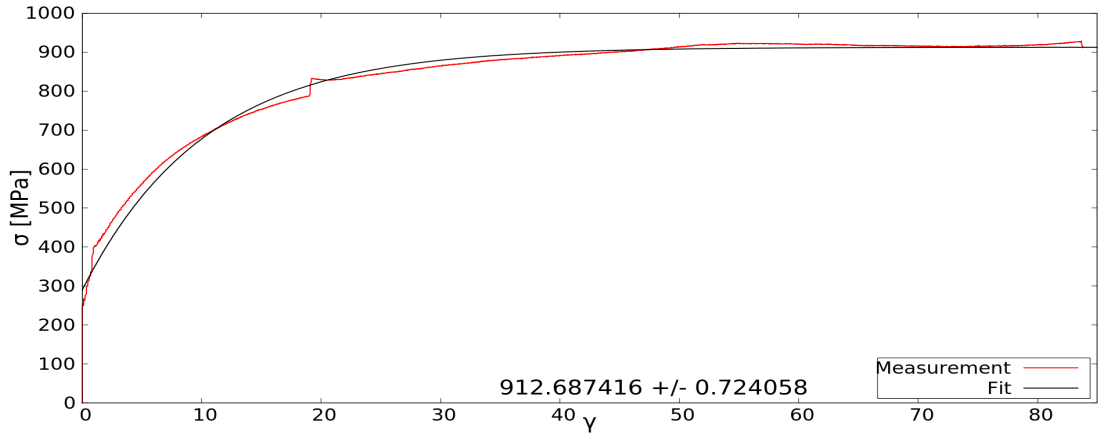

Figure A.24: Saturation curve fitted to the data from deformation # 5 at 1 $\frac{rot}{min}$ with the saturation stress value from the fit

A.6 6 Rotations per Second

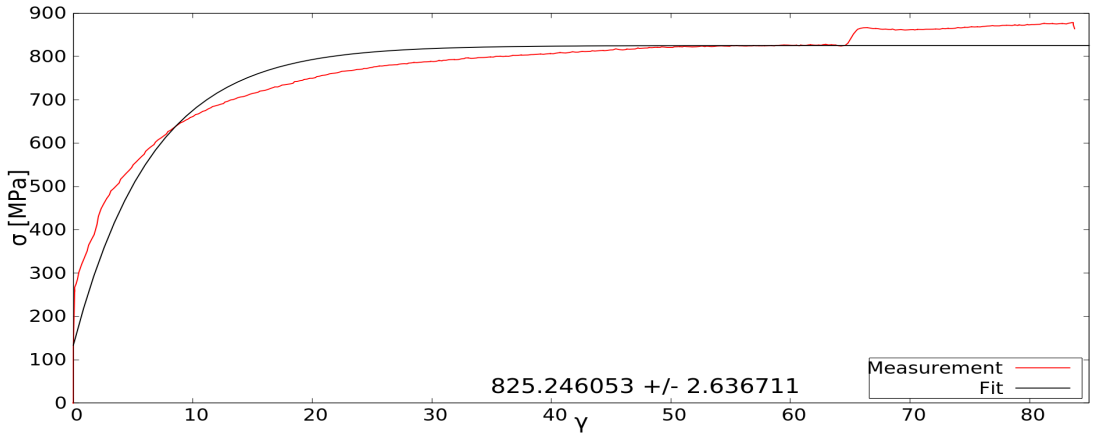

Figure A.25: Saturation curve fitted to the data from deformation # 1 at 6 $\frac{rot}{min}$ with the saturation stress value from the fit

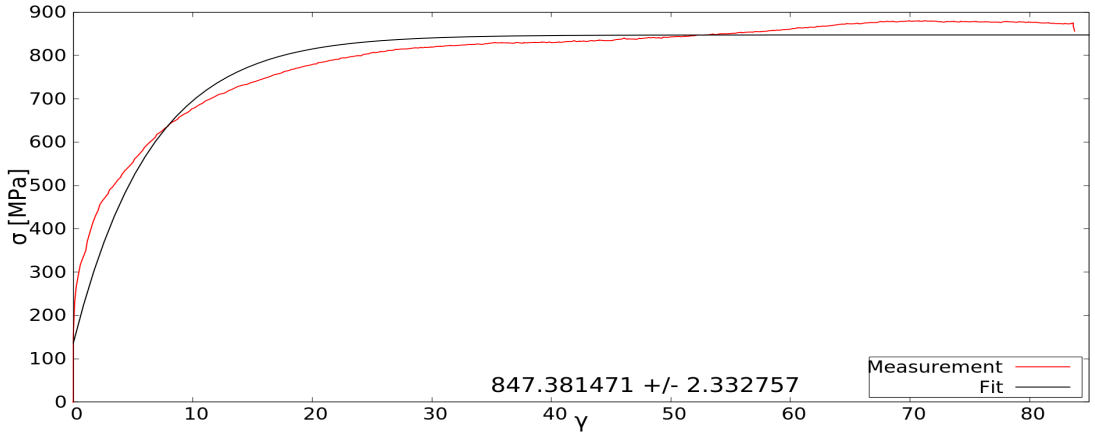

Figure A.26: Saturation curve fitted to the data from deformation # 2 at 6 $\frac{rot}{min}$ with the saturation stress value from the fit

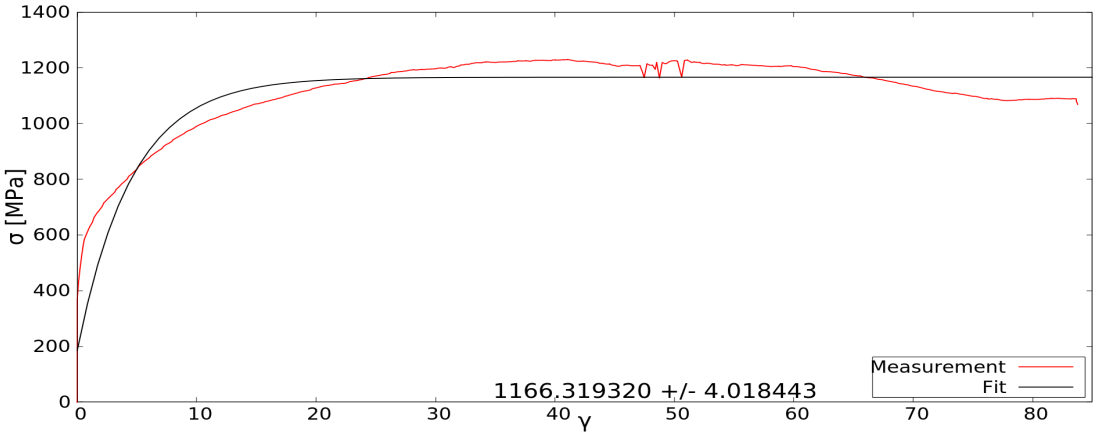

Figure A.27: Saturation curve fitted to the data from deformation # 3 at 6 $\frac{rot}{min}$ with the saturation stress value from the fit

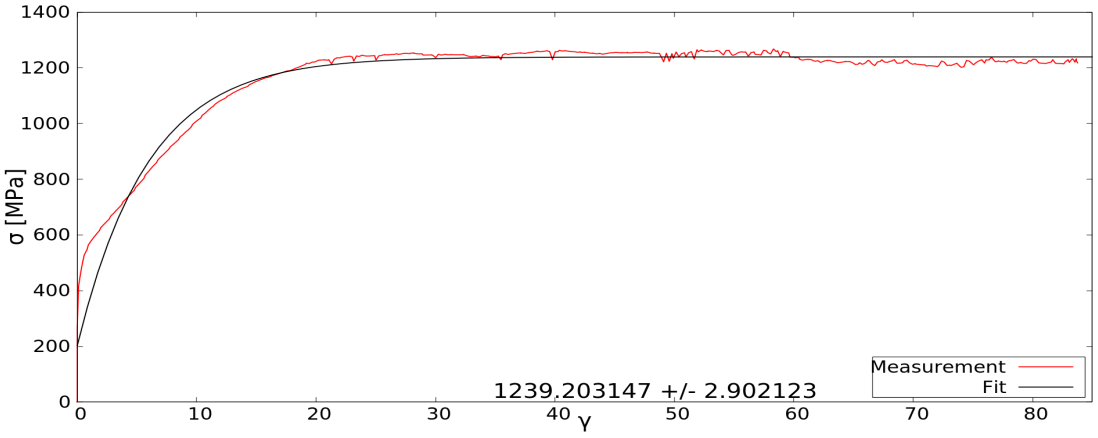

Figure A.28: Saturation curve fitted to the data from deformation # 4 at 6 $\frac{rot}{min}$ with the saturation stress value from the fit

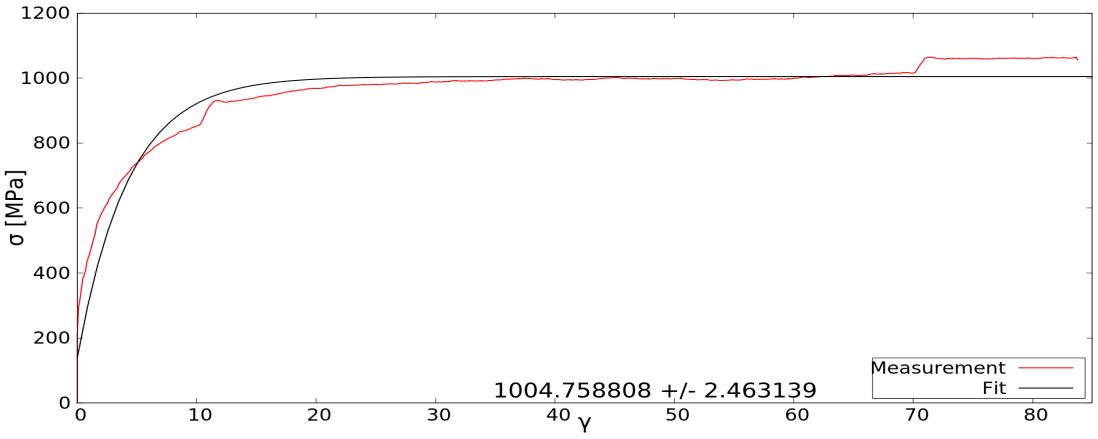

Figure A.29: Saturation curve fitted to the data from deformation # 5 at 6 $\frac{rot}{min}$ with the saturation stress value from the fit

Appendix B

Differential Scanning Calorimetry Measurements

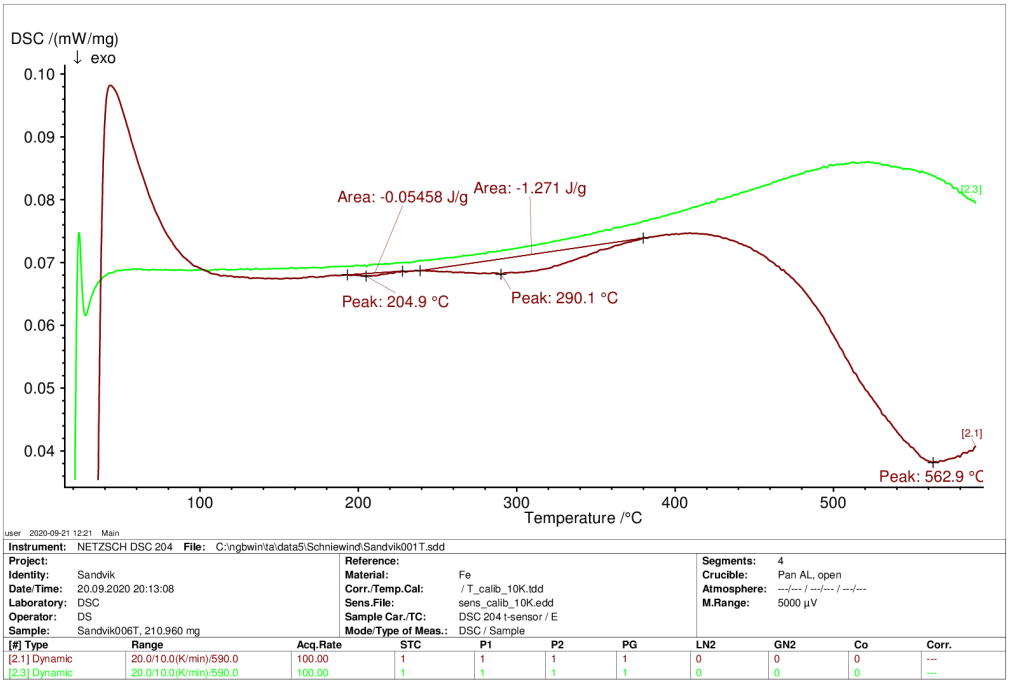

Figure B.1: DSC measurement curve of a sample deformed at 0.01 $\frac{rot}{min}$ with peak temperature and peak area

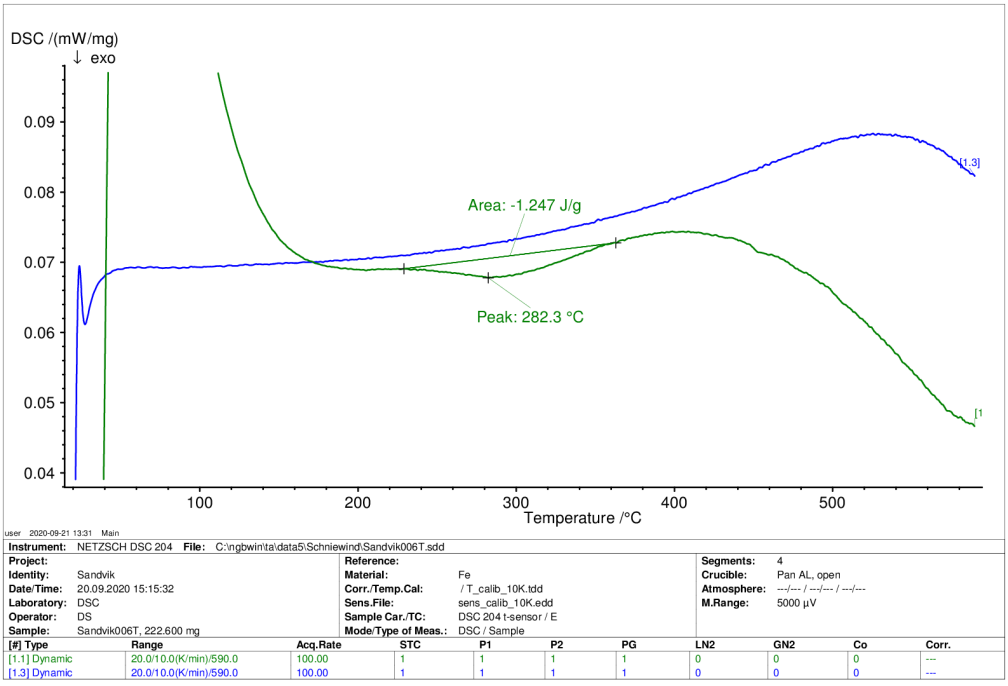

Figure B.2: DSC measurement curve of a sample deformed at 0.06 $\frac{rot}{min}$ with peak temperature and peak area

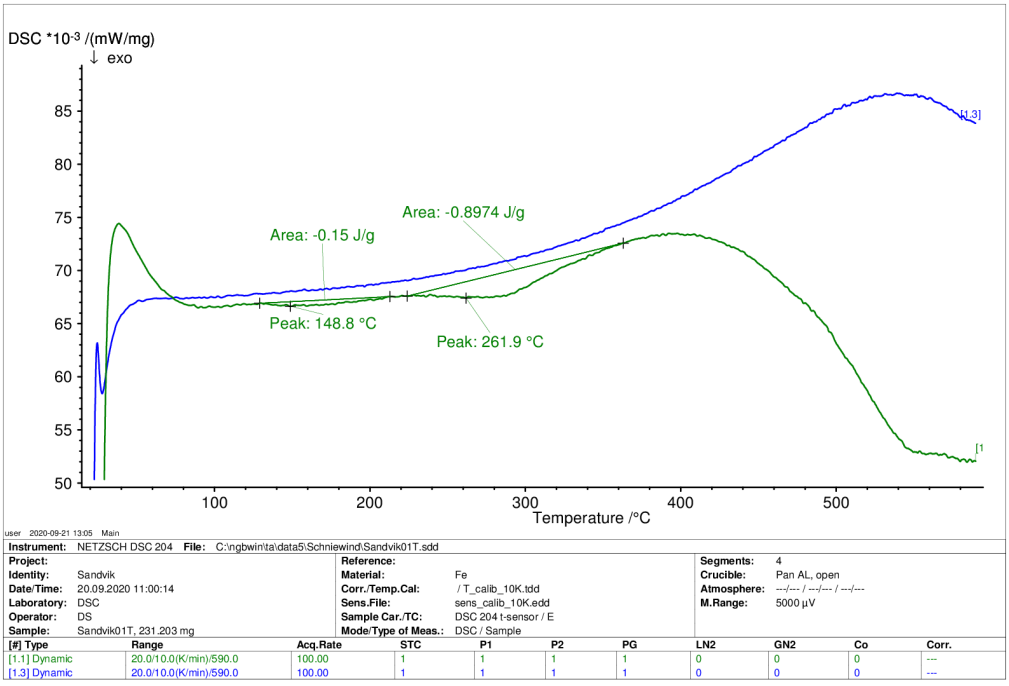

Figure B.3: DSC measurement curve of a sample deformed at 0.1 $\frac{rot}{min}$ with peak temperature and peak area

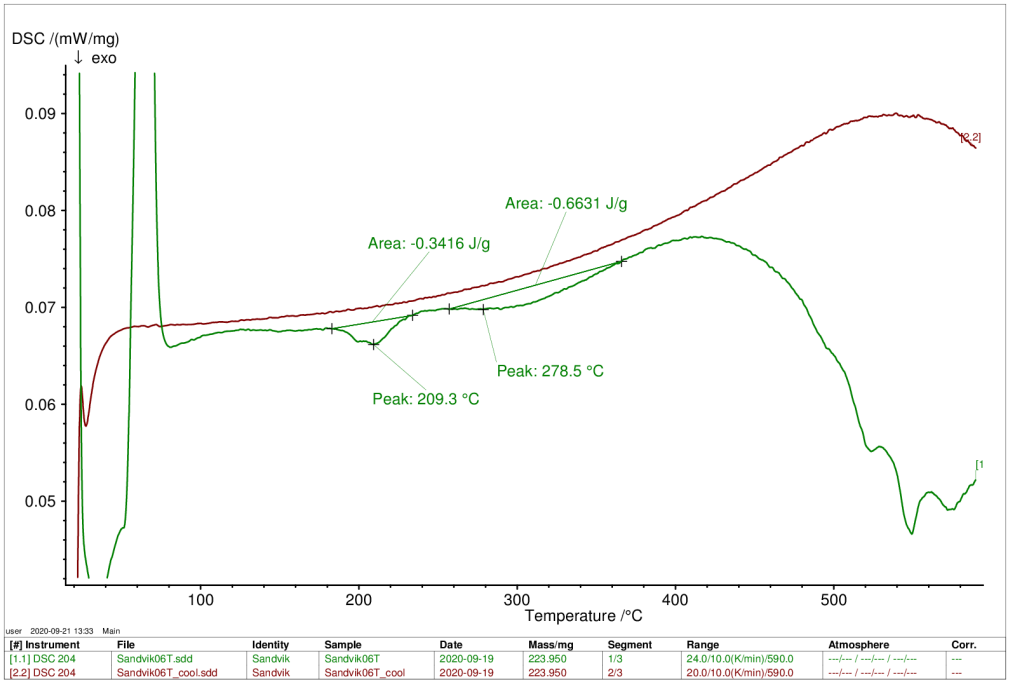

Figure B.4: DSC measurement curve of a sample deformed at 0.6 $\frac{rot}{min}$ with peak temperature and peak area

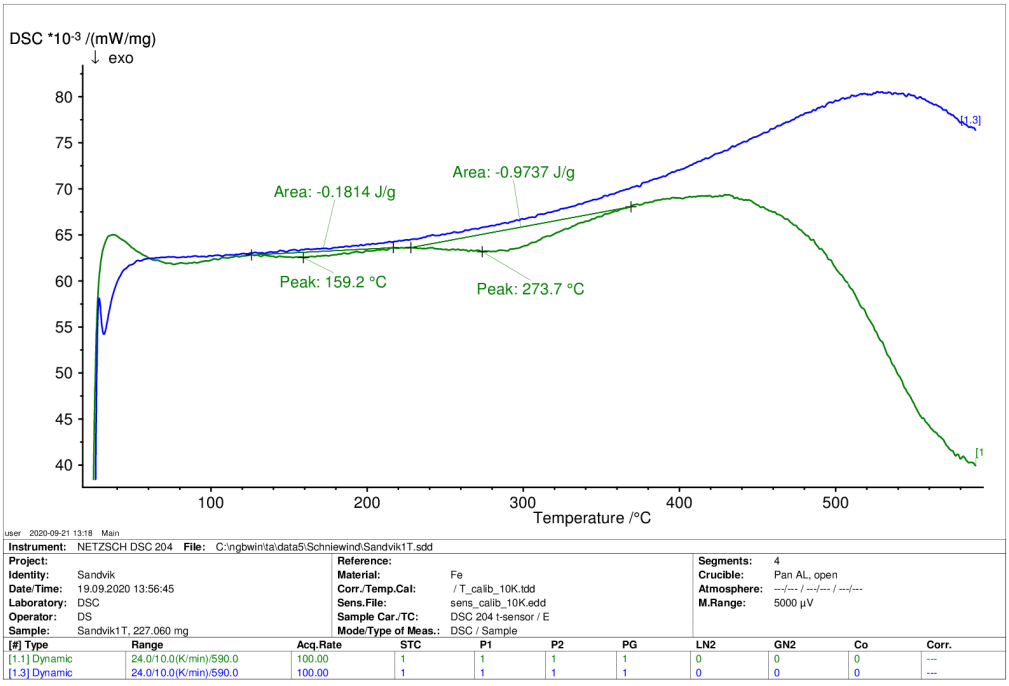

Figure B.5: DSC measurement curve of a sample deformed at 1 $\frac{rot}{min}$ with peak temperature and peak area

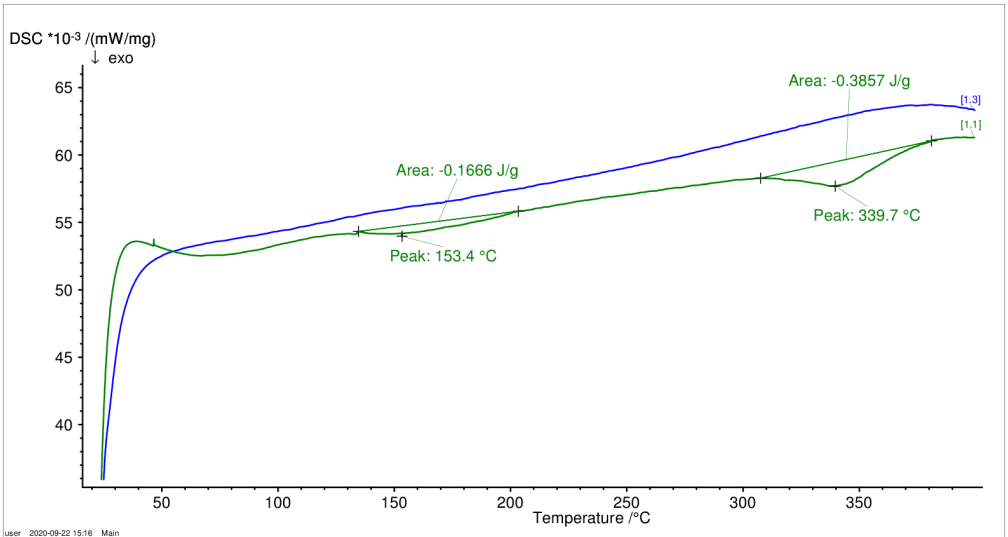

Figure B.6: DSC measurement curve of a sample deformed at 6 $\frac{rot}{min}$ with peak temperature and peak area